VELOCITY FLUCTUATIONS AND THEIR STATISTICS
IN TURBULENT CONVECTION

By

YI SHEN

Bachelor of Science

FuDan University

Shanghai, China

1989

Submitted to the Faculty of the
Graduate College of the
Oklahoma State University
in partial fulfillment of
the requirements for
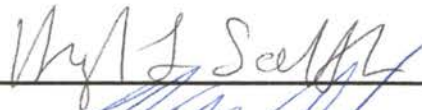the Degree of
DOCTOR OF PHILOSOPHY
May, 1996

VELOCITY FLUCTUATIONS AND THEIR STATISTICS
IN TURBULENT CONVECTION

Thesis Approved:

_____
Thesis Adviser

_____

_____

_____

Thomas C. Collins
_____
Dean of the Graduate College

ii

ACKNOWLEDGMENTS

TABLE OF CONTENTS

LIST OF FIGURES

CHAPTER I

INTRODUCTION

Turbulence is a phenomenon which occurs widely in nature and in many engineering systems. In the atmosphere, oceans, rivers, heat exchangers, and automobile engines, turbulence becomes a common feature and its importance is self-evident. The understanding of turbulence has long been a fundamental problem in physics. Since the pioneering work by Osborne Reynolds at the end of the nineteenth century, considerable progress has been made in understanding the nature of turbulence, which includes measurement of key parameters in turbulent flows, mathematical formulation, and numerical calculation of various turbulence problems. These studies have revealed that the problem of turbulence is, in fact, very difficult to solve because of its nonlinearility in its governing equations. Prof. George Carrier of Harvard University emphasized this point with the remark: "If, in the year 2000, someone delivers a lecture on fluid mechanics research in the next 50 years, he will probably start by noting that turbulence is our major unsolved problem" [5].

Because of the difficulties in finding the exact solutions for turbulent flows, many statistical methods have been utilized to study turbulence. In the past the results were more descriptive than quantitative. In 1940s Kolmogorov proposed a classical model [13] which describes the fully developed turbulence. In his model, turbulence is viewed as a cascade of turbulent kinetic energy from the largest eddies of size l_0 to smaller eddies with a constant energy flux ε. The cascade continues until the size of the eddies becomes comparable to the dissipation length $l_{\min}$. In the theory the Kolmogorov cut-off length $l_{\min} \sim l_0(\nu^3/\varepsilon)^{\frac{1}{4}}$, where ν is the kinematic viscosity of the fluid. According to Kolmogorov, only two parameters, l and ε, are

relevant to the small scale turbulence, when the length scale l is in the inertial range $l_{min} \ll l \ll l_0$. With a simple dimensional argument, one can show that the scaling velocity (or the eddy velocity) $u(l) \sim (\varepsilon l)^{\frac{1}{3}}$. The theory ignores the effect of boundaries and assumes the flow to be isotropic and homogeneous. However, in many real flows, boundaries are always finite and different coherent structures have been observed in systems. Many recent studies have been focused on how the kinematic energy is transported in real turbulent flows. There are two directions from which turbulence can be approached. One can start from the steady flows that are just barely unstable, and proceed through various states as the control parameter is increased. Or one can prepare the flow directly into a well developed turbulent state and study its putatively universal statistical properties.

An example is Rayleigh-Bénard convection, which is named after the first two scientists, Bénard (experimental study in 1901) and Rayleigh (theoretical calculation in 1916), who studied thermal convection system at the beginning of this century. When a horizontal layer of fluid is heated from below, Rayleigh-Bénard convection will occur if the temperature difference ΔT across the fluid layer exceeds a critical value ΔT_c. The control parameter in thermal convection is the Rayleigh number Ra, which is proportional to ΔT. In recent years much attention has been focused on Rayleigh-Bénard convection both in the chaotic regime, where Ra slightly exceeds a critical value Ra_c (proportional to ΔT_c), and in the turbulent regime where $Ra \gg Ra_c$. The recent discovery of scaling laws in the heat flux and temperature statistics in turbulent convection [6][39] shed new light on the nature of the convective turbulence. These experiments have stimulated considerable experimental [29] and theoretical efforts [18][22][23], aimed at explaining the observed scaling laws in the temperature field. The theoretical calculations arrive at similar conclusions for the temperature field, but have different assumptions and predictions for the velocity field in turbulent bulk regions and near viscous and thermal boundary layers. In contrast to the great number of temperature measurements, however, experimental information about velocity fluctuations and their statistics in turbulent convection is very limited. This motivated us to carry

out a systematic experimental study of the statistical properties of the velocity field in turbulent convection. With the direct measurements of velocity fluctuations and their statistics, we can verify the assumptions and test the predictions of various theoretical models [6][28]. The advantages of using Rayleigh-Bénard convection as an example to study turbulence are: (1) Rayleigh-Bénard convection has well defined boundary conditions; and (2) the change of turbulent states in thermal convection can be observed in a well controlled way (by controlling the Rayleigh number Ra).

The lack of the velocity information in turbulent convection is partially due to the fact that the conventional methods for measuring velocity, such as hot-wire anemometry and laser Doppler velocimetry (LDV), are not suitable for thermal turbulence (limitations will be discussed in Chapter III). To overcome the experimental difficulties, Tong, Xia, and Ackerson [36] have developed a new light scattering technique of incoherent cross-correlation spectroscopy (ICS) to measure the local velocity fluctuations and their statistics. This technique has the advantages of high spatial resolution, fast temporal response, and ease of use. In this thesis, we have used the ICS technique to study the statistical properties of the local velocity in turbulent convection. We have also exploited the technique of photon correlation spectroscopy (HCS) to measure the velocity difference at various length scales. These studies have found notable features of turbulent convection and have resulted in a series of publications [25][26][35].

This thesis is a summary of our light scattering study of turbulent Rayleigh-Bénard convection during the last five years. Chapter II briefly reviews the recent theoretical work. Experimental methods and apparatus appear in Chapter III, and our experimental results are discussed in Chapter IV. Finally the thesis is concluded in Chapter V.

CHAPTER II

BACKGROUND

In this chapter we review some background information about Rayleigh-Bénard convection and discuss recent theoretical models for turbulent convection.

Rayleigh-Bénard Convection

When a horizontal layer of fluid is heated from below, Rayleigh-Bénard convection will occur if the temperature difference ΔT across the layer exceeds a critical value ΔT_c. Because of the buoyancy effect due to gravity, the cooler fluid on the top of the fluid layer will start a downward motion and the warmer fluid on the bottom of the fluid layer will start its upward motion. Thus, a convection flow is established. As an incompressible fluid in a closed box, Rayleigh-Bénard convection can be described by the following equations of motion:

Incompressibility equation:

$$\nabla \cdot \mathbf{v} = 0; \tag{1}$$

Momentum equation:

$$(\frac{\partial \mathbf{v}}{\partial t} + \mathbf{v} \cdot \nabla \mathbf{v}) = \nu \nabla^2 \mathbf{v} - \nabla p / \rho_0 + \alpha \Delta T g \, \hat{z}. \tag{2}$$

Heat equation:

$$(\frac{\partial T}{\partial t} + \mathbf{v} \cdot \nabla T) = \kappa_d \nabla^2 T + \Phi, \tag{3}$$

where Φ denotes the dissipation function, due for example to viscous friction; for our experiments Φ is negligible. In the above, $\mathbf{v}$, p, and T are, respectively, the unknown velocity, pressure, and temperature fields, ρ_0 is the density of the fluid, g is the gravitational acceleration, ν is the kinematic viscosity, c_p is the specific

heat, κ_d the thermal diffusivity, $\alpha = \frac{1}{\rho}\frac{\partial \rho}{\partial T}$ is the thermal expansion coefficient, and $\Delta T = T_{bottom} - T_{top}$ is the temperature difference between the upper and lower plates. The vertical coordinate is denoted as $\hat{z}$ with the positive direction pointing upwards.

To get the above equations, we have used Boussinesq [38] approximation, in which all fluid properties, except for the density, are assumed to be temperature independent. The time averaged density variation is so small compared to the density itself that one may neglect its effect in all terms of the equations except for the buoyancy term. Eq. (1) is obtained from the mass conservation equation, $\frac{\partial \rho}{\partial t} + \nabla \cdot (\rho \mathbf{v}) = 0$, simplified under the Boussinesq approximation. Eq. (2) is the Navier-Stokes equation with the external force being the net buoyance force $\alpha \Delta T g \hat{z}$. Eq. (3) is the heat equation for thermal convection.

For turbulent convection, the unknown fields $\mathbf{v}$, p, and T are coupled together. Furthermore, the nonlinear operator $\mathbf{v} \cdot \nabla$ makes it very difficult to find exact solutions for the equations. However, there exists qualitative analysis which can shed some light on the problem. Using the temperature difference ΔT, the cell height h, and the typical thermal diffusion time h^2/κ_d as the scaling variables for the temperature T, the length L, and the time t, one may rewrite Eqs. (1), (2), and (3) in dimensionless forms:

$$\nabla \cdot \mathbf{v} = 0, \tag{4}$$

$$\frac{\partial T}{\partial t} + \mathbf{v} \cdot \nabla T = \nabla^2 T, \tag{5}$$

$$\frac{1}{P_r}\left(\frac{\partial \mathbf{v}}{\partial t} + \mathbf{v} \cdot \nabla \mathbf{v} + \nabla p\right) = \nabla^2 \mathbf{v} - Ra\hat{z}. \tag{6}$$

The boundary conditions are: (1) $\mathbf{v}_{sidewalls} = \mathbf{v}_{plates} = 0$, (nonslip condition); (2) $T_{top} = 1/2$, $T_{bottom} = -1/2$, (regulated temperature at the upper and lower plates); and (3) $(\nabla T \cdot \hat{n})_{sidewalls} = 0$ (no heat flux leakage at the sidewalls). Eq. (6) illustrates that solutions for the velocity $\mathbf{v}(\mathbf{x}, t)$, temperature $T(\mathbf{x}, t)$, and pressure $P(\mathbf{x}, t)$ only depend on the dimensionless Rayleigh number

$$Ra = \frac{\alpha g h^3 \Delta T}{\nu \kappa_d}, \tag{7}$$

and the Prandtl number

$$\mathrm{Pr} = \frac{\nu}{\kappa_d}. \tag{8}$$

Different fluids with the same values of Ra and Pr will have a similar flow behavior, because the fluid parameters enter the problem only through these two dimensionless numbers. The Rayleigh number can also be expressed as the ratio of the buoyancy contribution to the diffusion contribution,

$$Ra = \frac{\tau_t \tau_v}{\tau_b^2}, \tag{9}$$

where $\tau_t \sim h^2/\kappa_d$ is the thermal diffusion time, $\tau_v \sim h^2/\nu$ is the viscous diffusion time, and $\tau_b \sim (h/a)^{\frac{1}{2}} \sim (\frac{h}{g\alpha\Delta T})^{\frac{1}{2}}$ is the time for the buoyant force to move the fluid from the lower plate to the upper plate. When Ra is increased above the critical value $Ra_c \sim 10^3$, the buoyancy force overcomes the viscous and thermal diffusions, and the fluid starts to flow. In this case, the heat is transferred by convection other than the conduction. Similarly, the Prandtl number P_r can be expressed in terms of the ratio of thermal diffusion contribution to viscous diffusion contribution,

$$\mathrm{Pr} = \frac{\tau_t}{\tau_v}. \tag{10}$$

In convection experiments, both the Rayleigh number Ra and the Prandtl number P_r are well controlled. Because Ra can be easily changed in the experiment, most recent experimental studies have been focused on characterizing the flow states of the convection with different Ra. As Ra is increased from 10^3 to 10^{14}, the motion of the fluid undergoes several different phases from pure convection to turbulence (Figure 1). To characterize the flow states, a group of researchers led by Prof. Albert Libchaber at University of Chicago have carried out an experiment in which the Nusselt number Nu was measured as a function of Ra while keeping Pr constant. The Nusselt number Nu is the total heat flux, q_{total}, transferred vertically through the cell, normalized by the pure conductive heat flux $q_c = k_w \Delta T/h$, where k_w is the thermal conductivity of the fluid. Therefore, we have

$$Nu = \frac{q_{total}}{k_w \Delta T/h}. \tag{11}$$
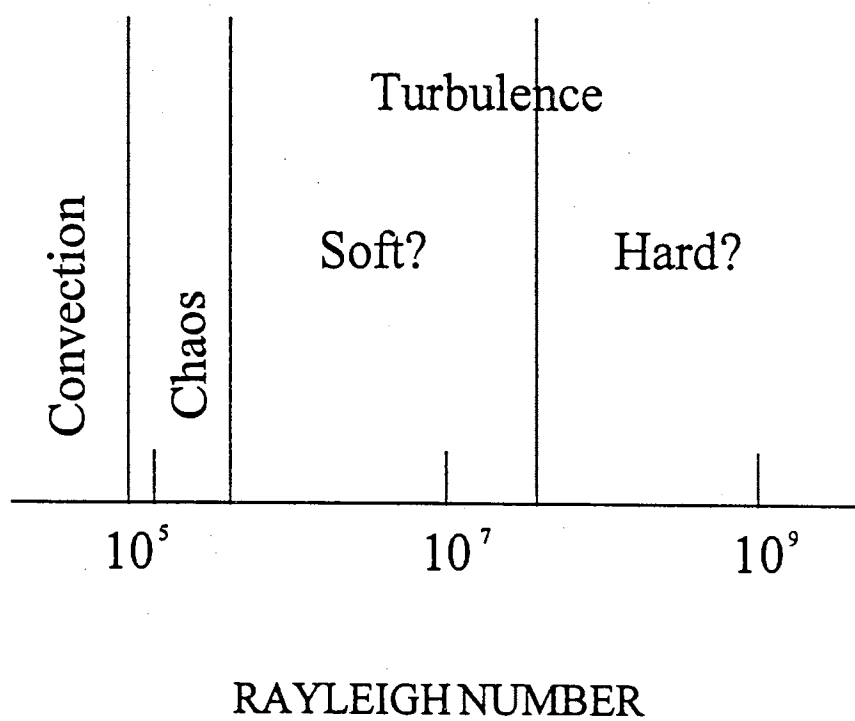
Figure 1. Flow states of thermal convection (From [31]).
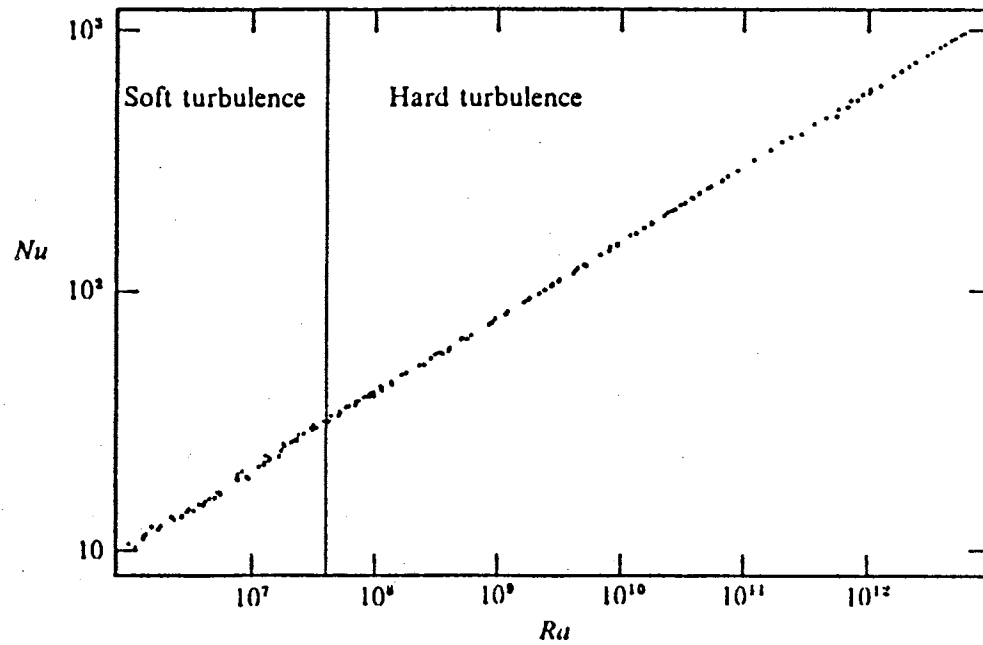
Figure 2. Nusselt number as a function of Rayleigh number, measured at the University of Chicago in a cell filled with helium. The curve has a slope of 1/3 in the region marked "soft turbulence," but the slope decreases to a value of 2/7 in the region marked "hard turbulence" (From [31]).

The experiment was performed in helium gas at $5°k$, and Figure 2 shows the measured Nu vs. Ra curve. As shown in the Figure 2, the heat transported by convection is increased as the flow gets more and more turbulent. The Chicago group has found that turbulent convection can be further classified into two states : "soft" turbulence and "hard" turbulence (details will be given later). The Rayleigh number, which separates the two states is approximately $Ra \sim 4 \times 10^7$. In our convection experiment in water, Ra is varied in the range between 10^7 and 10^{11}. In this Ra range, fluid motion starts at the upper end of the "soft" turbulence regime and extends well into the "hard" turbulence regime.

The local velocity u, which is a function of position and time, may also change with Rayleigh number. In turbulent convection, the Reynolds number Re is often used as the dimensionless velocity. The Reynolds number is defined as

$$Re = \frac{(\mathbf{v} \cdot \nabla)\mathbf{v}}{\nu \nabla^2 \mathbf{v}} \simeq \frac{ul}{\nu}, \tag{12}$$

where u is a typical velocity and l is the characteristic size of the related turbulent flow. As shown in Eq. (12), the Reynolds number Re measures the relative importance of the nonlinear advection term to the viscous term in Eq. (6). The Peclet number Pe is also used as the dimensionless velocity. The Peclet number Pe, which is defined as

$$Pe = Re \, Pr = \frac{(\mathbf{v} \cdot \nabla)T}{\kappa_d \nabla^2 T} \simeq \frac{ul}{\kappa_d}, \tag{13}$$

gives the ratio of the temperature advection to the thermal diffusion. When the Prandtl number $P_r \sim 1$, which is the case for convection experiments in water, the Reynolds number and the Peclet number are essentially the same.

A Brief Introduction To Turbulence

In the above, the word "turbulence" has been mentioned again and again. But what exactly is "turbulence?"

There is no simple definition for turbulence. A commonly used definition is that turbulence is a chaotic motion both in time and in space. Some characteristics of turbulent flows are:

(1) Irregularity. This makes the deterministic approach to turbulence problems very difficult.

(2) Turbulent diffusivity. This enhances the mixing and transferring of mass, momentum, and heat.

(3) Large Reynolds numbers. This introduces the instability of flows.

(4) Three dimensional vorticity fluctuations.

(5) Dissipation. A constant supply of energy is required.

Because of the difficulties of finding the exact solution for turbulent flows, one often relies on dimensional analysis and other statistical methods to analyze turbulent flows. When a flow property, such as temperature or velocity, only depends on a few independent variables, one may use a dimensional analysis to qualitatively predict a relationship between the control parameters and the flow property concerned. An example is the $\frac{5}{3}$ law of the energy spectrum developed by Kolmogorov in the 1940s [13]. The energy spectrum E(k) is defined as the kinetic energy per unit mass and per unit wavenumber k. In the Kolmogorov theory, the turbulent energy is assumed to cascade from large scales to small scales as illustrated in Figure 3. After the turbulent flow reaches a steady state, the energy is injected into the flow at the largest scale $\sim l_0$ (the largest eddy) and then is transferred successively to smaller eddies of sizes $\sim l_1$, $\sim l_2$, $\cdots$ until the dissipation cut-off length $l_{\min}$ is reached. The smaller eddies are exposed to the strain-rate field of the larger eddies. By increasing their vorticity, the smaller eddies gain their own energy at the expense of the energy of the larger eddies. As a result, there is an energy flux, ε, transferred from the larger eddies to the smaller ones. For simplicity, Kolmogorov theory assumes that $\varepsilon_n \simeq \varepsilon$ is a constant. The kinematic energy per unit mass associated with the nth generation of the eddy l_n is

$$E(n) = \int_{k_n}^{k_{n+1}} E(k)dk, \tag{14}$$

where $k_n \sim l_n^{-1}$ is the relevant wave number. In the above, the eddy energy

$$E(n) \sim u_n^2, \tag{15}$$
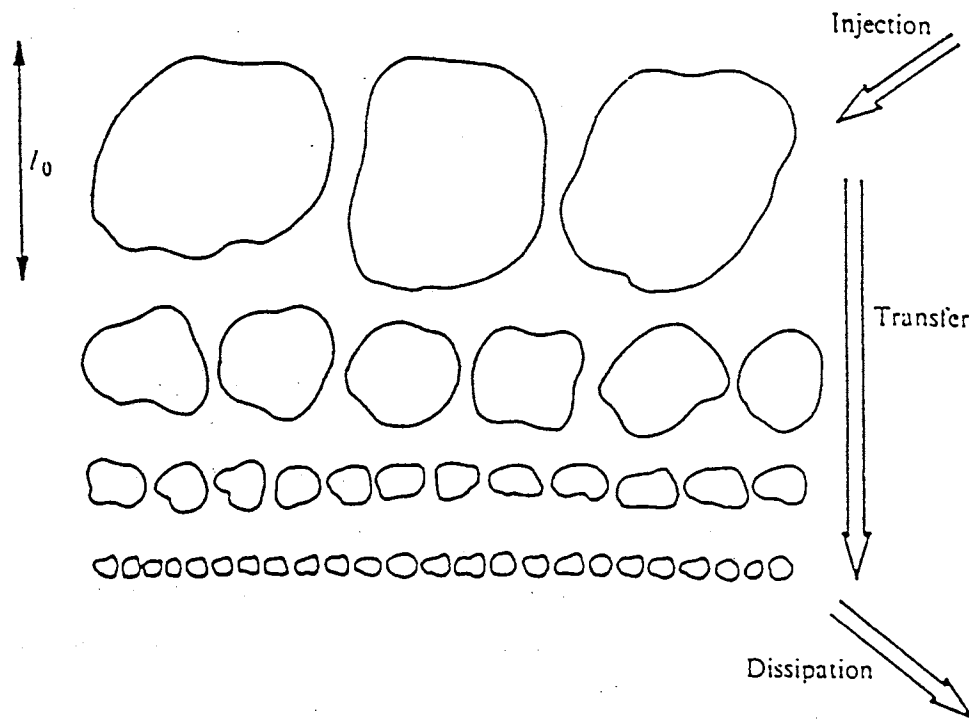
Figure 3. The energy cascade according to the 1941 Kolmogorov theory.

where u_n is the characteristic velocity of the eddy l_n. It should be pointed out that u_n is rather a typical velocity difference $u_n = \delta v(l_n)$ across a distance l_n, than a mean flow velocity. Therefore the eddy turn over time is given by

$$t_n \sim \frac{l_n}{u_n}. \qquad (16)$$

This relation will not apply to the two extreme cases at the beginning of the cascade and at the end of it. At the largest scale l_0, the cascade is not local and $t_0 = l_0/u_o$ should be used as the time scale. At the end of the cascade, the energy transfer is no longer able to compete with the dissipation. The thermal and viscous dissipation times can be estimated as

$$t_{vis} \sim \frac{l_{min}^2}{\nu}, \qquad (17)$$

and

$$t_{ther} \sim \frac{l_{min}^2}{\kappa_d}. \qquad (18)$$

At the length scale l_{min}, the kinetic energy will dissipate into heat, and the eddies can not further cascade into any smaller sizes. In accordance with the time range $t_{diss} \gg t_n \gg t_0$, there exists an inertial range, $l_{min} \ll l_n \ll l_0$, in which one may ignore the dissipation and the boundary effect. In this inertial range,

$$\varepsilon \sim \varepsilon_n \sim \frac{E_n}{t_n} \sim \frac{u_n^3}{l_n}, \qquad (19)$$

then we have

$$u_n = u(l_n) \sim (\varepsilon l_n)^{\frac{1}{3}}, \qquad (20)$$

and

$$E_n \sim (\varepsilon l_n)^{\frac{2}{3}}. \qquad (21)$$

After the Fourier transformation, Eq. (21) yields the Kolmogorov spectrum [14]

$$E(k) \sim \varepsilon^{\frac{2}{3}} k^{-\frac{5}{3}}. \qquad (22)$$

Another useful method for the study of turbulence is the asymtotic invariance analysis. This method approaches turbulence as the control parameter goes to

infinity. For turbulent convection, the extreme high Rayleigh number could be achieved by letting the height of the convection cell go to infinity, while fixing the temperature difference between the upper and lower plates. The original theory for turbulent boundary layers was developed using the asymptotic approach. For turbulent convection, it has been observed that the average temperature gradient $\frac{\partial T}{\partial z}$ is concentrated mainly in thin thermal boundary layers near the upper and lower plates [1]. The flow at the center of the cell is homogeneous and the central region is an isothermal region, as shown in Figure 4 (for SF_6 at $Ra = 4.8 \times 10^7$, $\Delta = 16.3°C$, and $h = 15.2\,cm$. The inset shows an enlargement of the region close to the plate). Then it is natural to define the thermal boundary layer thickness δ as

$$\frac{\Delta T/2}{\delta} = \left(\frac{\partial T}{\partial z}\right)_{at\ plate,} \tag{23}$$

where the $\Delta T/2$ is used to preserve the symmetry of the upper and lower thermal boundary layers. Using the scaling approach, we have

$$\delta \sim h\ Ra^{-\beta}. \tag{24}$$

The thickness of the thermal layer will reach a finite limit even when the height of the cell and thus the Rayleigh number go to infinity. In this case the thermal boundary layer at the upper plate does not communicate with that at the lower plate. The only value for β, which makes δ independent of the cell height, is $1/3$ since $Ra \sim h^3$. With the definition of Nu in Eq. (11), we may relate the Nusselt number with the boundary layer thickness δ by equating the total heat flux transferred through the cell with that just out of the thermal boundary layer:

$$q_{total} = k_w \left(\frac{\partial T}{\partial z}\right)_{at\ plate.} \tag{25}$$

Therefore, we have

$$Nu = \frac{h}{2\delta}. \tag{26}$$

Because Nu can be measured with little technical difficulty and great accuracy, Eq. (26) has become a useful way to estimate the thermal boundary layer thickness
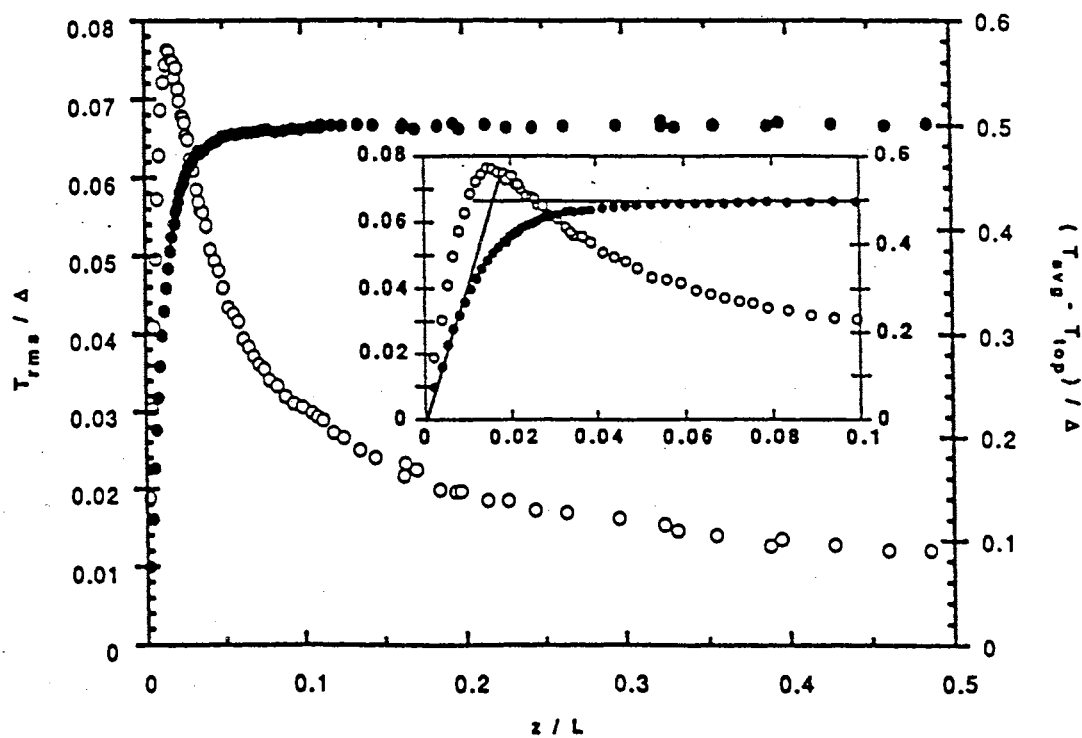
Figure 4. The normalized mean (black dots) and rms (open dots) temperature profiles vs z/L (from [1]).

δ. From Eqs. (24) and (26), one obtains an important power law in the classical theory of thermal convection:

$$Nu \sim Ra^{\beta}, \tag{27}$$

with $\beta = 1/3$. With the critical Rayleigh number $Ra_c = 1870$, one can even estimate the amplitude in Eq. (27) as

$$Nu \sim (\frac{Ra}{Ra_c})^{\frac{1}{3}} = 0.04\, Ra^{\frac{1}{3}}. \tag{28}$$

Besides the power law dependence in $Nu\,(Ra)$, the RMS values of the temperature and velocity fluctuations at the cell center have also been expressed in power law functions of Ra. The characteristic temperature scale δT_c (i.e., the RMS value) varies with the Rayleigh number,

$$\frac{\delta T_c}{\Delta T} \sim Ra^{\gamma}, \tag{29}$$

The calculated values for γ varies among different models, from $-\frac{1}{3}$ to $-\frac{1}{9}$ [16][19][20]. The characteristic velocity u_c in the central region (or the corresponding Reynolds number) increases with the Rayleigh number according to

$$\frac{u_c h}{\nu} \sim Ra^{\omega}. \tag{30}$$

The value of ω has been estimated as $\sim 1/2$ in the classical theory of turbulent convection [13].

Do the scaling exponents in Eqs. (20), (27), (29), and (30) accurately describe the temperature and velocity statistics in turbulent convection? Many experimental studies have been carried out to examine the Rayleigh number dependence of the Nusselt number. Perhaps the experiments carried out by the Chicago group, that we mentioned in the last section, represent the most accurate results in the temperature measurements [12]. The Chicago experiment has found that (1) in "soft" turbulence regime, in which Ra is in the range between 5×10^5 and 4×10^7, the relation $Nu \sim Ra^{\frac{1}{3}}$ holds; and (2) when in the "hard" turbulence regime ($Ra > 4 \times 10^7$), the measured Nu can be well described by a power law

$$Nu = 0.23 \times Ra^{0.282 \pm 0.006} \sim Ra^{2/7}. \tag{31}$$

The obtained power law in Eq. (31) differs from Eq. (28) not only in the power law amplitude but also the exponent. Another important difference between the soft turbulence and the hard turbulence is that their temperature probability density functions (PDF) have different functional forms: in the soft turbulence regime, the temperature PDF at the cell center has a Gaussian form, whereas in the hard turbulence regime, the temperature PDF is of an exponential form. Figs. 5 ($Ra = 8.41 \times 10^6$) and 6 ($Ra = 1.47 \times 10^8$) show the measured temperature PDFs in the Chicago experiment. In this experiment the value of the exponent γ in Eq. (29) is found to be $\gamma = -0.147 \simeq -1/7$.

In contrast to the great number of temperature measurements, experimental information about the velocity field in turbulent convection is very limited. In this thesis we study the statistical properties of the velocity field in turbulent convection. In one experiment [35], we have used the technique of homodyne photon correlation spectroscopy to measure the velocity difference $u(l)$ over varying length scale l. It is found that the relative velocity $u(l) \sim l^{3/5}$, which is different from the Kolmogorov prediction $u(l_n) \sim l_n^{\frac{1}{3}}$ shown in Eq. (20). The 3/5 exponent for velocity scaling is the Bolgiano scaling exponent [4][22]. In turbulent convection, the energy cascade gives rise to different size eddies and these eddies can convert different amounts of kinematic energy to potential energy in the gravitational field. Energy flux ε is no longer a constant because of this leak. Only entropy flux still is conserved in this case [18]. The l-dependence of ε gives the $l^{3/5}$ dependence of velocity difference $u(l)$. Using the technique of incoherent cross-correlation spectroscopy, which is recently developed by Tong, Xia, and Ackerson, we also measured the PDF of the local velocity at the cell center [25]. The experiment reveals that the value of the exponent ω in Eq. (30) is $\omega = 0.44$ (we will discuss the experimental details in Chapter IV).

Large-Scale Circulation And Thermal Plumes

There are two main coherent structures involved in turbulent convection. They are: (1) the coherent large-scale circulation near the boundaries of the cell;
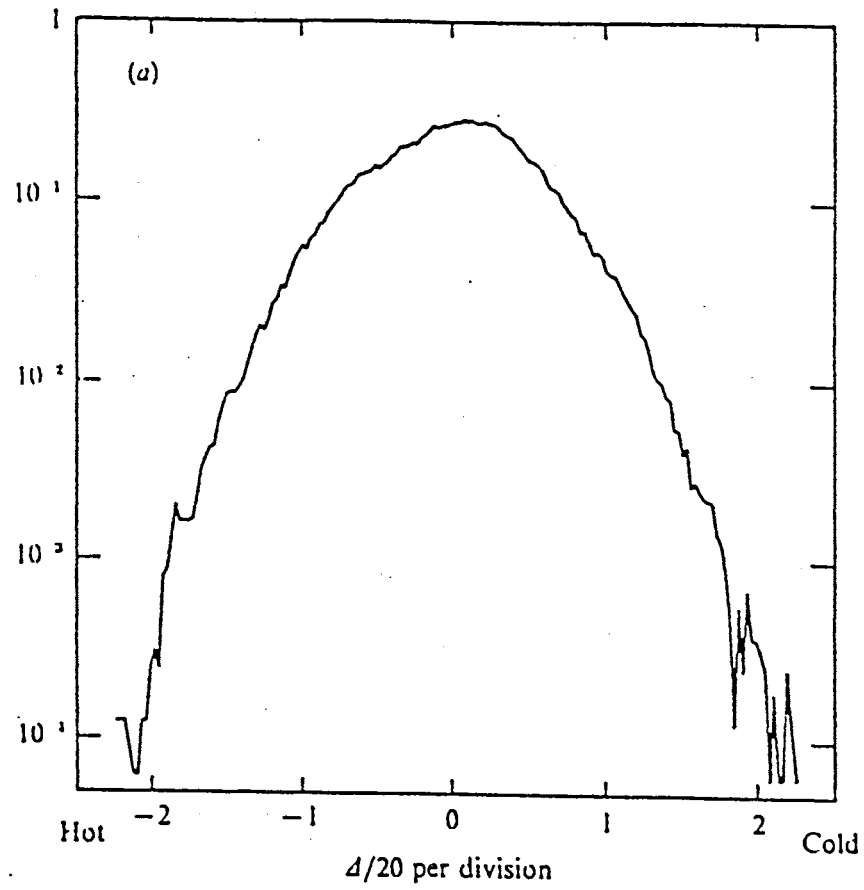
Figure 5. Histogram of the temperature distribution in soft turbulence regime.

(b)

Hot

Cold

$\Delta/20$ per division
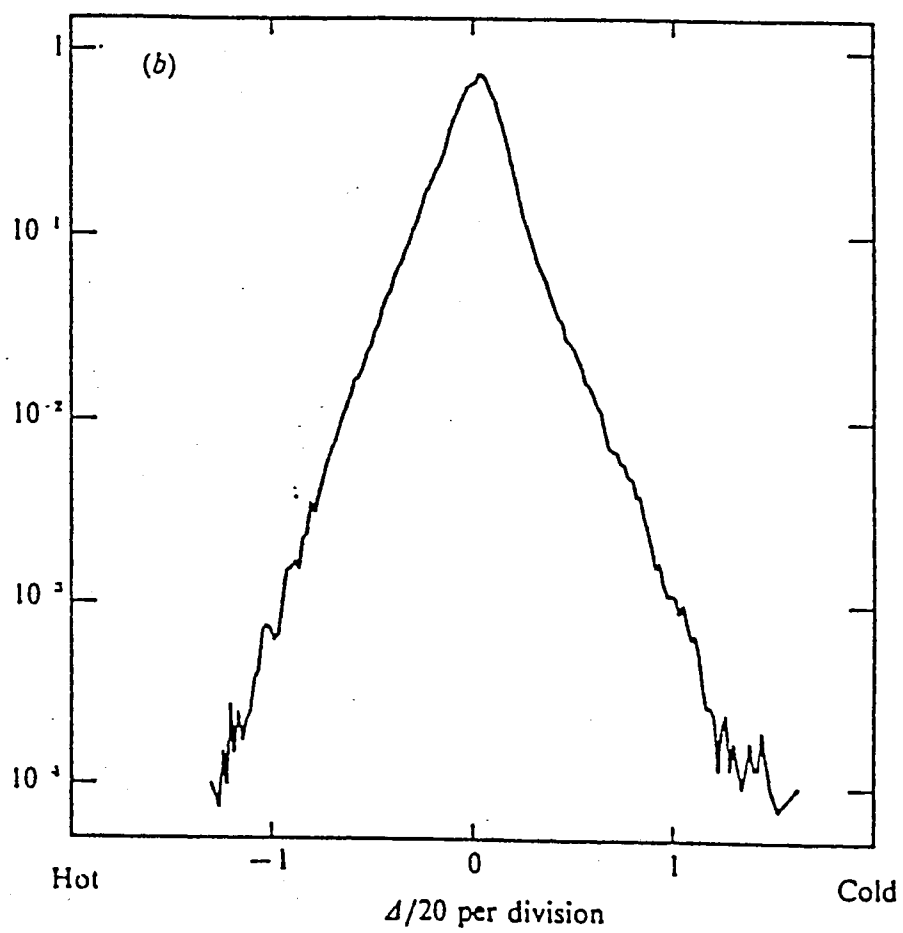
Figure 6. Histogram of the temperature distribution in hard turbulence regime.

and (2) intermittent bursts of thermal plumes from the thermal boundary layers. The large scale circulation is also called wind when it is near the upper and lower plates and its size is comparable with the cell height h. Thermal plumes and the large-scale circulation, which modifies the boundary layers via its shear, are found to coexist in a closed convection cell [24][40]. The two salient features of turbulent convection are directly related to the transport of heat and momentum across the cell, and have been adopted in several theoretical models [28]. A central unanswered question in the study of turbulent convection is which coherent structure dominates the heat transport in turbulent convection? The large-scale circulation or the thermal plumes?

Kadanoff and coworkers developed a scaling model to derive the non-classical values of the exponents β, γ, and ω in the hard turbulence regime. Their model involves thermal plumes but ignores the large-scale circulation completely. It is assumed that the convective heat flux equals the conductive heat flux near the thermal boundary layers. The heat is transported through the central region of the cell by thermal plumes with a typical velocity u_c and temperature T_c. In this case, we have

$$H \sim u_c T_c. \tag{32}$$

To match the boundary layer with the turbulent core region, it is further proposed that there is a mixing zone in between the two regions, whose thickness h_{mix} satisfies the condition $\delta < h_{mix} \ll h$. In the mixing zone the thermal plumes break off from the boundary layer, accelerate to certain velocity, and merge into the flow in the central region. For strong turbulent mixing, thermal diffusion can be ignored. With a simple dimensional argument, one can estimate the velocity of the plumes at the center to be proportional to the free-fall velocity,

$$u_c \sim (\alpha g \triangle T h)^{\frac{1}{2}}. \tag{33}$$

On the other hand, u_c may be considered as the maximum velocity of the plumes, at which the buoyancy force is balanced by the viscous forces. Therefore, we have

$$u_c \sim \frac{\alpha g \triangle T \, \delta^2}{\nu}. \tag{34}$$

Substituting Eqs. (26), (27), (29), and (30) into Eqs. (32), (33), and (34), one finds the scaling exponents β, γ, and ω

$$\beta = \gamma + \omega; \tag{35}$$

$$\gamma = 2\omega - 1; \tag{36}$$

$$\omega = 1 - 2\beta. \tag{37}$$

The final solutions for the above equations are: $\beta = 2/7$; $\gamma = -1/7$; and $\omega = 3/7$.

These values are in excellent agreement with the experimental results: $\beta = 0.283$, $\gamma = -0.147$, and $\omega = 0.44$, which were discussed in the last section. However a recent experiment shows [2] that a large part of the heat is carried by the large-scale circulation motion near the side wall of the cell. This is contrary to the assumption by Kadanoff et al. that the heat is transported through the central region by thermal plumes. In accordance with the new experimental result, Shraiman and Siggia proposed a different model [27], which ignores the effect of the thermal plumes on the heat transport assuming the thermal boundary layers lie within the shear layers. It is assumed in the model that the heat is carried mainly by the large-scale circulation, which moves horizontally near the upper and lower surfaces and vertically near the side-walls of the convection cell. In this case,

$$NuRa \sim< (\nabla v)^2 > . \tag{38}$$

Similar to the velocity profile in a turbulent pipe flow and other open turbulent flows, the velocity profile $v(z)$ in the closed convection cell as a function of the distance from the lower (or upper) plate is assumed to have the logarithmic form

$$v = u_*(2.5\ln(z/z_*) + 5), \tag{39}$$

with

$$z_* = \frac{\mathrm{Pr}}{u_*}, \tag{40}$$

and where the characteristic velocity u_* is related to large-scale Reynolds number by

$$u_* = \frac{\mathrm{Pr}\, Re}{2.5(\ln(u_*/\mathrm{Pr}) + 6)}. \tag{41}$$

With Eqs. (38), (39), (40), and (41), one can show that [28]

$$Nu \sim Ra^{2/7} f_1(\text{Pr}, A), \tag{42}$$

and

$$Re \sim Ra^{3/7} f_2(\text{Pr}, A),$$

where $f_1(\text{Pr}, A)$ and $f_2(\text{Pr}, A)$ are functions of the Prandtl number Pr and the aspect ratio A, respectively. Although the model by Shraiman and Siggia uses different assumptions for the mechanism of the heat transport, its solutions for the scaling exponents β and ω are the same as those obtained by Kadanoff and coworkers.

To examine the effect of the large-scale circulation on the heat transport, Solomon and Gollub [29] have carried out an experiment, which used a moving boundary of mercury to enhance the large-scale circulation near the lower thermal boundary layer. The Nusselt number Nu was found to increase by as much as 70% with water being the convection fluid. This increase in the heat flux could be attributed to the enhanced large-scale circulation. However, some theoretical calculations have suggested that though the large-scale flow plays an important role in the heat transport, it is impossible for the large-scale circulation to carry all the heat in turbulent convection. The point is partially supported by the fact that the shear velocity in the experiment by Solomon and Gollub was much larger than that in the natural convective flow.

Inspired by the recent studies of turbulent convection, we have conducted a novel convection experiment in a closed cell with rough surfaces on both the upper and lower plates. The vertical heat flux is found to be increased by 20%, when the Rayleigh number becomes larger than a transition value. The experiment reveals that the main effect of the surface roughness is to increase the emission of large thermal plumes, which travel vertically through the central region. These extra thermal plumes enhance the heat transport, and they are also responsible for the anisotropic behavior of the velocity fluctuations at the cell center. Our experiment suggests both the large-scale circulation and the thermal plumes contribute to

the heat transport in turbulent convection. There may well be a middle ground between the model by Kadanoff et al. in which the large-scale circulation is ignored, and the model by Shraiman and Siggia, in which the thermal plumes play no role in the heat transport.

CHAPTER III

MEASUREMENT METHODS AND APPARATUS

Rayleigh-Bénard Cell

The convection cell used in the experiment was a vertical cylindrical cell with an inner diameter of 20 cm, and it is shown in Figure 7. The upper and lower plates were made of brass and their surfaces were electroplated with a thin layer of gold. The sidewall of the cell was a cylindrical ring made of transparent Plexglas to admit the incident light in the horizontal direction and transmit the scattered light. There was a filling stem at the center of the upper plate and the vertical incident light could go through the stem. The cylindrical cell can smooth out some undesirable velocity fluctuations, which could be produced by the corners of a square cell. Four cylindrical rings with heights of 6.6, 13.2, 20, and 40 cm were used, respectively, to extend the accessible range of Ra. In our experiments, Ra was varied between 10^7 and 10^{11}. The corresponding aspect ratios ($A = diameter/height$) for these cells are 3.0, 1.5, 1.0, and 0.5, respectively.

To regulate the temperature of the upper plate, we used a cooler and a circulator (both from NESLAB) to pump $2°C$ water through the cooling chamber fitted on the top of the upper plate. The lower plate was heated uniformly at a constant rate by two circular silicone rubber heaters (Model SRFR 7/10 from OMEGA). The two heaters were sandwiched in between two copper plates on the back side of the lower plate and were sealed with conducting grease to ensure a uniform heating. The electric resistance of each heater was 33.4Ω, and the total resistance of the two parallel-connected heaters was 16.7Ω. The electric current going through the heaters was provided by a dc power supply with 0.1% long-term stability. Two OMEGA 44031 thermistors were embedded in the upper and lower
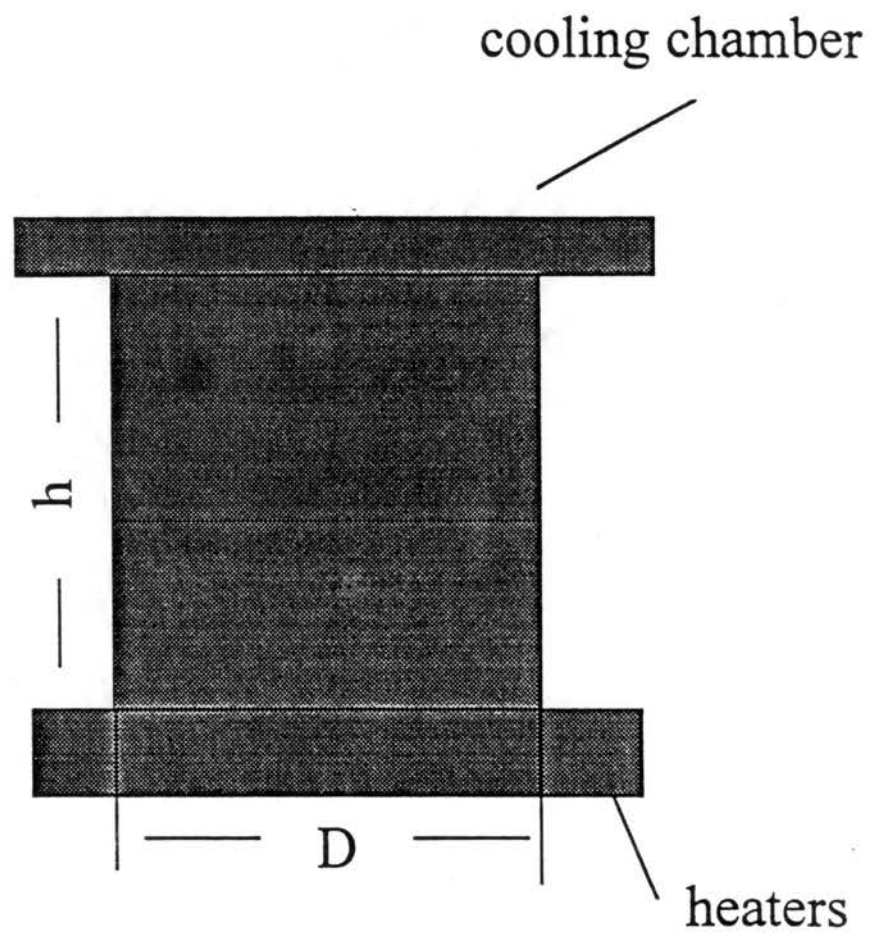
Figure 7. Thermal convection cell with $A = 1$.

plates, respectively, and they were used to record the temperature of both plates. At the beginning of the whole project, we checked the temperature distribution of the upper and lower plates. It was found that the temperature at different points on the upper plate was uniform within $0.1°C$ for any given Ra. Similar temperature uniformity was also achieved on the lower plate. The temperature difference between the upper and lower plates, was varied between $4°C$ and $50°C$. The control parameter in the convection experiment is the Rayleigh number $Ra = \alpha g h^3 \Delta T / \nu \kappa_d$, with α being the thermal expansion coefficient, g the gravitational acceleration, h the height of the convection cell, ΔT the temperature difference between the upper and lower plates, ν and κ_d the kinematic viscosity and the thermal diffusivity of the convecting fluid (water), respectively. Water was chosen as the convecting fluid because its molecular properties (α, ν, and κ_d) at different temperatures are well documented and it is easily available in the laboratory.

Thermal measurements were conducted to study the heat transport in turbulent convection. The heat transport is measured by the Nusselt number Nu, which is the ratio of the total vertical heat flux across the cell to the heat flux carried by conduction. In our experiment, the total heat flux across the cell was determined by the electric power, V_e^2/R, required to keep the lower plate at a constant temperature. Here V_e is the dc voltage applied to the heaters and $R = 16.7\Omega$ is the total resistance of the heating circuit. Because the heat flux by conduction is $\kappa_w \Delta T / h$, the Nusselt number then becomes $Nu = \frac{V^2 h}{R \Delta T \kappa_w}$. In the heat transport measurements, the convection cell was well insulated by a square box made of gold fiber glass to prevent heat leakage. The insulation box is not shown in Figure 7 for a better view of other components in the setup. The heat flux measurements were carried out in both the "smooth cell" and the "rough cell". The upper and lower plates for the rough cells were made of the same brass plates as those used in the smooth cells, but had woven V-shaped grooves on them. The grooves had a vertex angle of 90° and their spacing was such that a square lattice of pyramids was formed on the surface. The height of the pyramids (the roughness height h_0)

was 3.175 mm and their spacing s =6.35 mm. Both the smooth and rough brass plates were electroplated with a thin layer of gold to prevent corrosion in the fluid.

The cell was filled with distilled water, which was seeded with monodispersed polymer latex spheres. We used 0.14 μm diameter latex particles in the measurement of velocity differences and 0.95 μm diameter particles in the measurement of local velocity fluctuations. These particles had a high surface charge density to ensure their stability in the convecting fluid. The density of the particles is very close to that of water, so that they can faithfully follow the fluid motion. The volume fraction of the seed particles used in our experiments was between 10^{-5} and 10^{-7}. At these particle concentrations, the mean spacing between the seed particles is much larger than their diameter (dilute solution) but much smaller than the smallest turbulent scale (sufficient sampling).

To completely characterize a turbulent flow, one needs to measure the pressure, the temperature and the velocity fields, simultaneously. The pressure field is perhaps the most difficult one to measure, because the spatial resolution and the response time of currently available pressure sensors (piezoelectric transducers) are limited. Semiconductor thermistors and cold wires are commonly used in the temperature measurements. The conventional methods for measuring velocity are hot-wire anemometry and laser Doppler velocimetry (LDV). However, these two techniques are not suitable for the study of thermal convection. This is because large temperature fluctuations in thermal convection may ruin the calibration of a hot-wire anemometer. Strong fluctuations of the fluid refractive index due to temperature fluctuations can cause the two laser beams used in LDV to wander and defocus in the fluid. This corruption of laser beam properties will reduce the signal-to-noise level of LDV. While visualization techniques are still useful in recognizing flow patterns, they have limited spatial resolution and statistics for the velocity measurement. After reviewing all the experimental methods available, we decided to use two new light scattering methods in our study of turbulent convection. The technique of homodyne correlation spectroscopy (HCS) was used to measure the velocity differences over various length scales. A newly developed

technique of incoherent cross-correlation spectroscopy was used to measure the local velocity and its PDF. In the following three sections, we will discuss details of these experimental methods.

Scattering From Seed Particles

A good starting point is to consider the scattering of N identical particles in the fluid. Figure 8 shows a schematic diagram of the scattering geometry. Let a plane wave $E_0 \exp[i(\mathbf{k_0} \cdot \mathbf{r} - \omega_0 t)]$ illuminate the scattering sample. Here $\mathbf{k_0}$ is the incident wave vector, ω_0 is the angular frequency, and E_0 is the amplitude of the incident wave. The incident field induces a radiating dipole moment in each of the particles. The total electric field $E(t)$ at a distance R from the sample is a sum of the fields radiated by each of the particles, and has the form

$$E(t) = \sum_{j=1}^{N} E_0' \exp[i\phi_j(t) - i\omega_0 t]. \tag{43}$$

Here E_0' is the amplitude of the field scattered by each of the particles, and is independent of the position of the particles. It is given by

$$E_0' = E_0[\exp(i\mathbf{k_s} \cdot \mathbf{R})/R](\omega_0/c)^2(\alpha - \alpha_0)V \sin\psi, \tag{44}$$

where $\mathbf{k_s}$ is the scattering wave vector, c is the speed of the light, ψ is the angle between the polarization direction of E_0 and the propagation direction of the scattered wave $\mathbf{k_s}$, $\alpha - \alpha_0$ is the dipole polarizability difference between the particle and the solvent, and V is the volume of the scattering particle. The phase factor $\phi_j(t)$ in Eq. (43) is $2\pi/\lambda$ (λ is the wavelength of the incident light) times the difference in path length between the jth particle and the origin O. Thus when R is at a large distance from the scattering region, we have

$$\phi_j(t) = \mathbf{q} \cdot \mathbf{r}_j(t), \tag{45}$$

where $\mathbf{r}_j(t)$ is the position of the jth particle. The momentum transfer vector $\mathbf{q}$, whose magnitude is $(4\pi n/\lambda)\sin\frac{\theta}{2}$, is a vector difference between the incident and

Cell

Incident
wave
front

K_0

O

jth

r_j

K_s

θ

detector

Scattered
wave
front
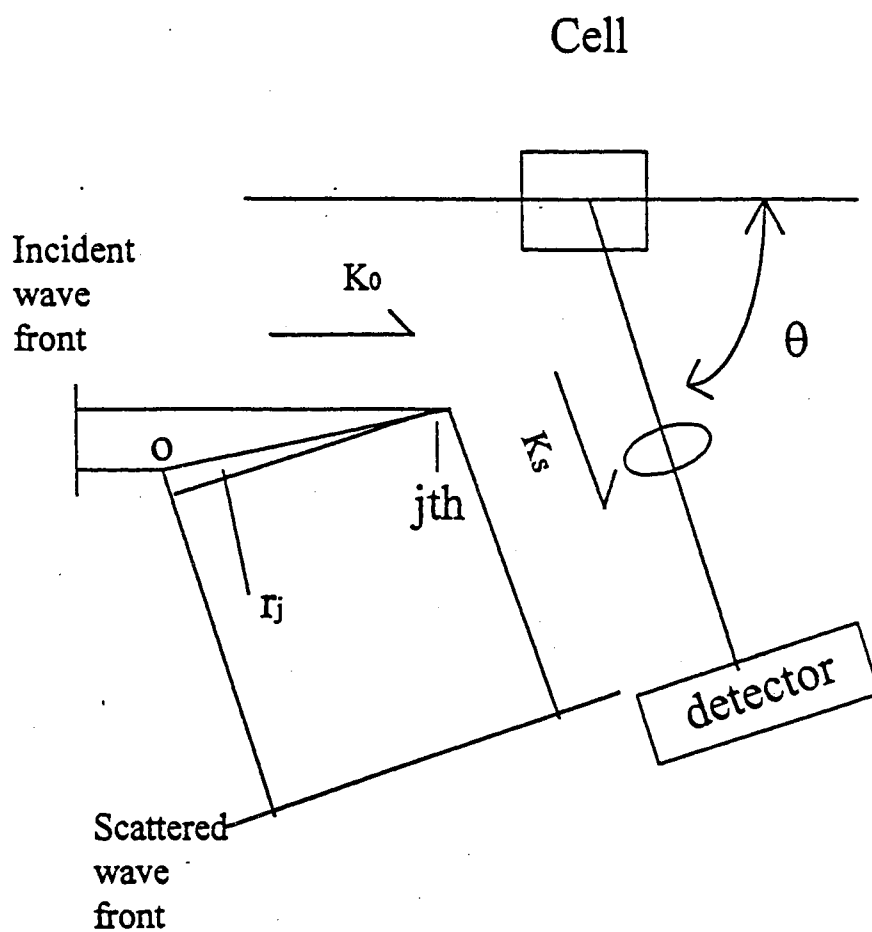
Figure 8. Schematic diagram of light scattering from seed particles.

scattered wave vectors. In the above, n is the refractive index of the solvent and θ is the scattering angle.

When the polarization of the incident wave is perpendicular to the scattering plane, the total electrical field scattered by isotropic particles has a simple form,

$$E(t) = C e^{-i\omega_0 t} \sum_{j=1}^{N} e^{i\phi_j(t)}, \tag{46}$$

where C is a proportionality constant, which is associated with the particle scattering ability.

The cross-correlation function of the scattering intensity is defined by

$$g_c(t) = \frac{< E_b^*(0)E_b(0)E_g^*(t)E_g(t) >}{< E_b^*(0)E_b(0) >< E_g^*(0)E_g(0) >} = \frac{K}{Q_b Q_g}, \tag{47}$$

where the angle brackets represent a time average. In the above, E_b and E_g are the scattered electric fields from the same laser source. In our experiment the laser beam consists of the blue and green lights, which are from a argon-ion laser operated under the multiline mode. When the laser is operated under the single line mode, $E_b = E_g$ and the green light ($\lambda = 514.5\,nm$) is used. Substituting Eq. (46) into Eq. (47), we have the normalized scattering intensity $Q_b = Q_g = Q$ with

$$Q = \sum_{i,j}^{N} < e^{-i\mathbf{q}\cdot[\mathbf{r}_i(t)-\mathbf{r}_j(t)]} >, \tag{48}$$

and

$$K = \sum_{i,j,k,l}^{N} < e^{-i\{\mathbf{q}_b\cdot[\mathbf{r}_i(0)-\mathbf{r}_j(0)]+\mathbf{q}_g\cdot[\mathbf{r}_k(0)-\mathbf{r}_l(0)]\}} e^{-i\mathbf{q}_g\cdot\int_0^t dt'\{\mathbf{v}[\mathbf{r}_k(t')]-\mathbf{v}[\mathbf{r}_j(t')]\}} > . \tag{49}$$

In the above, $\mathbf{q}_b$ and $\mathbf{q}_g$ are the momentum transfer vectors for the blue light and the green light, respectively. In Eq. (49) we have used the fact that

$$\mathbf{r}_i(t) = \mathbf{r}_i(0) + \int_0^t dt' \mathbf{v}[\mathbf{r}_i(t')], \tag{50}$$

where $\mathbf{v}[\mathbf{r}_i(t')]$ is the local velocity at position $\mathbf{r}_i(t')$, and the particles are assumed to follow the motion of the fluid.

Because the seed particles are randomly distributed in the fluid, the fluctuation terms ($i \neq j$) in Eq. (48) do not survive a time or ensemble average.

Then we have $Q = N_{avg}$, where N_{avg} is the average number of the particles in the scattering volume and the particle scattering power has been normalized to unity. With the same spirit, the fluctuation terms in Eq. (49) may also be dropped, and the remaining terms in Eq. (49) must satisfy the condition $\mathbf{q}_b \cdot [\mathbf{r}_i(0) - \mathbf{r}_j(0)] + \mathbf{q}_g \cdot [\mathbf{r}_k(0) - \mathbf{r}_l(0)] = 0$. The possible choices to satisfy the condition are

(1) $i = j = k = l$, for arbitrary nonzero $\mathbf{q}_b$ and $\mathbf{q}_g$;

(2) $i = j \neq k = l$, for arbitrary nonzero $\mathbf{q}_b$ and $\mathbf{q}_g$;

(3) $i = l \neq j = k$, for $\mathbf{q}_b = \mathbf{q}_g = \mathbf{q} \neq 0$;

(4) $i = k \neq j = l$, for $\mathbf{q}_b = -\mathbf{q}_g = \mathbf{q} \neq 0$.

Equation (47) then can be written as

$$g_c(t) = \frac{< N(0)N(t) >}{N_{avg}^2} + \frac{1}{N_{avg}^2} \sum_{i \neq j} < e^{-i\mathbf{q} \cdot \int_0^t dt' \{\mathbf{v}[\mathbf{r}_k(t')] - \mathbf{v}[\mathbf{r}_j(t')]\}} >, \qquad (51)$$

where $N(t)$ is the number of particles in the scattering volume at time t. The condition (1) ($i = j = k = l$) gives rise to the first term in Eq. (51), and the conditions (3) and (4) ($i = l \neq j = k$ and $i = k \neq j = l$) result in the second term in Eq. (51). Two assumptions have been made in getting Eq. (51). First, we dropped all the terms in Eq. (49) which satisfy the condition (2) ($i = j \neq k = l$), since rotation does not make any difference for isotropic particles in the dilute solution. Second, the number of the particles in the scattering volume changes with time, because the fluid motion carries the seed particles in and out of the laser beam.

Eq. (51) can be rewritten as

$$g_c(t) \simeq 1 + g_N(t) + g_{coh}(\vec{q}_b = \pm\vec{q}_g, t), \qquad (52)$$

with

$$g_N(t) = \frac{< \delta N(0)\delta N(t) >}{N_{avg}^2}, \qquad (53)$$

and

$$g_{coh}(t) = \frac{1}{N_{avg}^2} \sum_{k \neq j}^{N_{avg}} < e^{-i\mathbf{q} \cdot \int_0^t dt' \{\mathbf{v}[\mathbf{r}_k(t')] - \mathbf{v}[\mathbf{r}_j(t')]\}} > . \qquad (54)$$

In the above, $\delta N(t) = N(t) - N_{avg}$ is the number fluctuation, and a second order term $(\sim \frac{1}{N_{avg}^2})$ is ignored in Eq. (52). Because $< N(0)\,N(t) >$ in Eq. (53) goes as N_{avg}, we have $g_N(t) \sim \frac{1}{N_{avg}}$. In Eq. (54) the sum has $N(N-1) \sim N^2$ terms, and thus $g_{coh}(t) \sim 1$. In the experiment, $g_N(t)$ and $g_{coh}(t)$ can be measured separately by controlling the number of the particles in the scattering volume. With the different N_{avg}-dependence in $g_N(t)$ and $g_{coh}(t)$, one can measure the velocity difference and the local velocity in a turbulent flow. We now discuss experimental details of the two scattering methods.

Measurement Of Velocity Differences At Various Length Scales

In studies of turbulence, it is of great interest to measure the velocity difference $\delta \mathbf{v}(\mathbf{R}) = v(\mathbf{r}) - \mathbf{v}(\mathbf{r} + \mathbf{R})$ at various length scale R. In our experiment, $\delta \mathbf{v}(\mathbf{R})$ is measured by the technique of homodyne correlation spectroscopy (HCS). With this technique, the laser is operated under the single color mode (λ =514.5 nm), so that $\mathbf{q}_b = \mathbf{q}_g = \mathbf{q}$. According to Eq. (52), the measured correlation function is $g_c(t) = 1 + g_N(t) + g_{coh}(q,t)$. In the experiment, we carefully adjust the particle concentration so that $N_{avg} \gg 100$. In this case, $g_N(t)$ $(\sim \frac{1}{N_{avg}})$ has a much smaller magnitude than $g_{coh}(t)$, and the decay of $g_N(t)$ is at least ten times slower than that of $g_{coh}(t)$. Therefore, $g_N(t)$ in Eq. (52) can be omitted, and $g(t) = 1 + b\,g_{coh}(q,t)$, with $b \leq 1$ being an instrumental constant, whose value depends on the experimental setup.

Figure 9 shows the physical arrangement for the HCS experiment with the incident beam being in the horizontal direction. The incident beam was from a 4-W argon-ion laser (Coherent Innova-304), which was under the single-line operation with $\lambda = 514.5$ nm. The lens L_1 (its focus length f = 15 cm) focused the laser beam at the center of the convection cell. The focused beam had a typical diameter of 0.1 mm. The lens L_2 then projected the image of the scattering beam onto the slit S, whose width could be varied from 0.1 to 1.3 mm. Three lenses with focal lengths of 3, 8, and 20 cm were used in order to vary the magnification. With the combination of the three magnifications and the range of the slit widths, the real
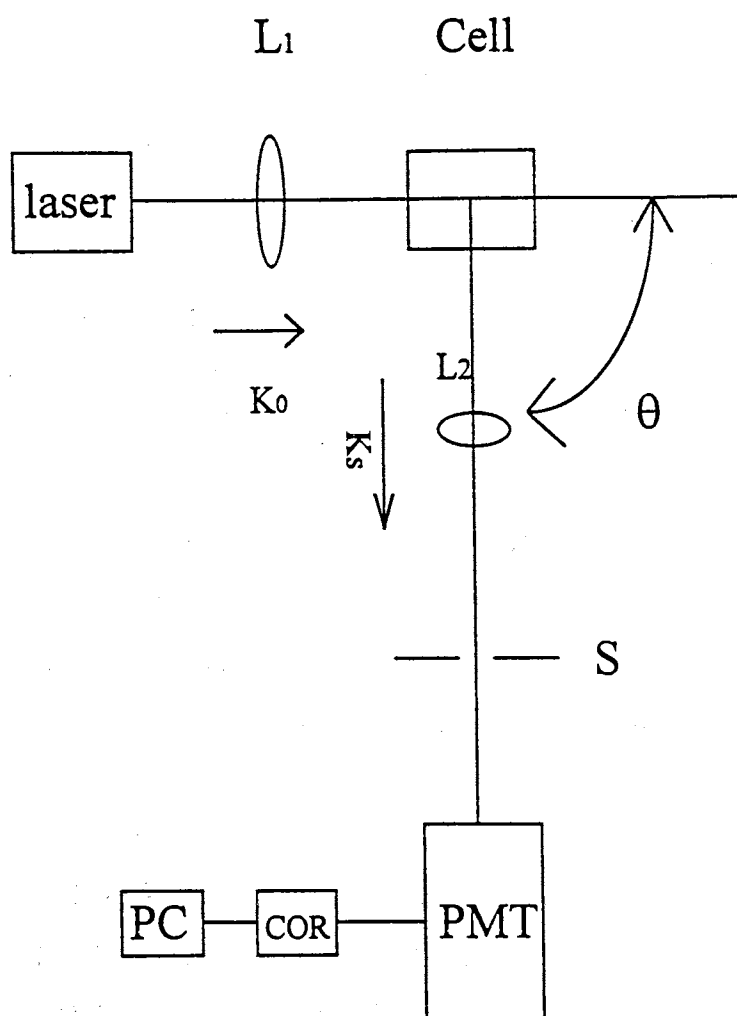
Figure 9. Schematic diagram of HCS setup (horizontal beam orientation).

length L of the thin cylindrical scattering volume viewed by the photo-detector was varied between 0.1 and 17 mm. The length L determines the maximum measurable eddy size, to which the auto-correlation function $g(t)$ is sensitive. Light passing through the slit fell on the photomultiplier (PMT), which recorded the time-varying intensity $I(t)$. The photomultiplier was located far behind the slit ($\sim 130\,cm$), so that light was collected from roughly one coherence area. In the measurement of the L-dependence of the velocity difference $u(L)$, the scattering angle θ was fixed at 90°. To measure the q-dependence of the correlation function $g(t)$, the lens L_2, the slit S, and the photomultiplier PMT were placed on a rotation track, with which one could change the scattering angle θ from 25° to 110°. The corresponding change of the momentum transfer vector, $q = (4\pi n/\lambda)\sin(\theta/2)$, was from 7.0×10^4 to $2.3 \times 10^5\,cm^{-1}$.

Figure 10 shows the physical arrangement of the HCS experiment with the incident beam in the vertical direction. The setup is similar to that shown in Figure 9. The polarizer P was added to align the polarization direction of the laser beam. Mirrors m_1, m_2, and m_3 were used to convert the horizontal beam into a vertical incident beam in the z direction. In this setup, the scattering angle θ was fixed at 90°.

As will be shown later in the experiment, the shortest turbulent eddy turnover time, t_L, is much longer than the typical decay time for $g_{coh}(t)$. In this case, one can replace the integral in Eq. (54) with $\delta v(\mathbf{R}, t')t$, where $\mathbf{R} = \mathbf{r}_l - \mathbf{r}_k$, and $\delta v(\mathbf{R}, t') = v[\mathbf{r}_k(t')] - v[\mathbf{r}_k(t') + \mathbf{R}]$. The summation in Eq. (54) can be replaced by an integration over the scattering volume, which is a line segment of length L. When the particles are grouped into pairs, we can rewrite Eq. (52) as

$$g(t) = 1 + \int_0^L dR\, h(R) < \cos[\mathbf{q} \cdot \delta v(\mathbf{R}, t')t] >_{t'}, \qquad (55)$$

where $h(R)$ is the number fraction of particle pairs separated by a distance R in the scattering volume L, and $< \cos[\mathbf{q} \cdot \delta v(\mathbf{R}, t')t] >_{t'}$ denotes a time average over t' [33]. One can easily show [33] that

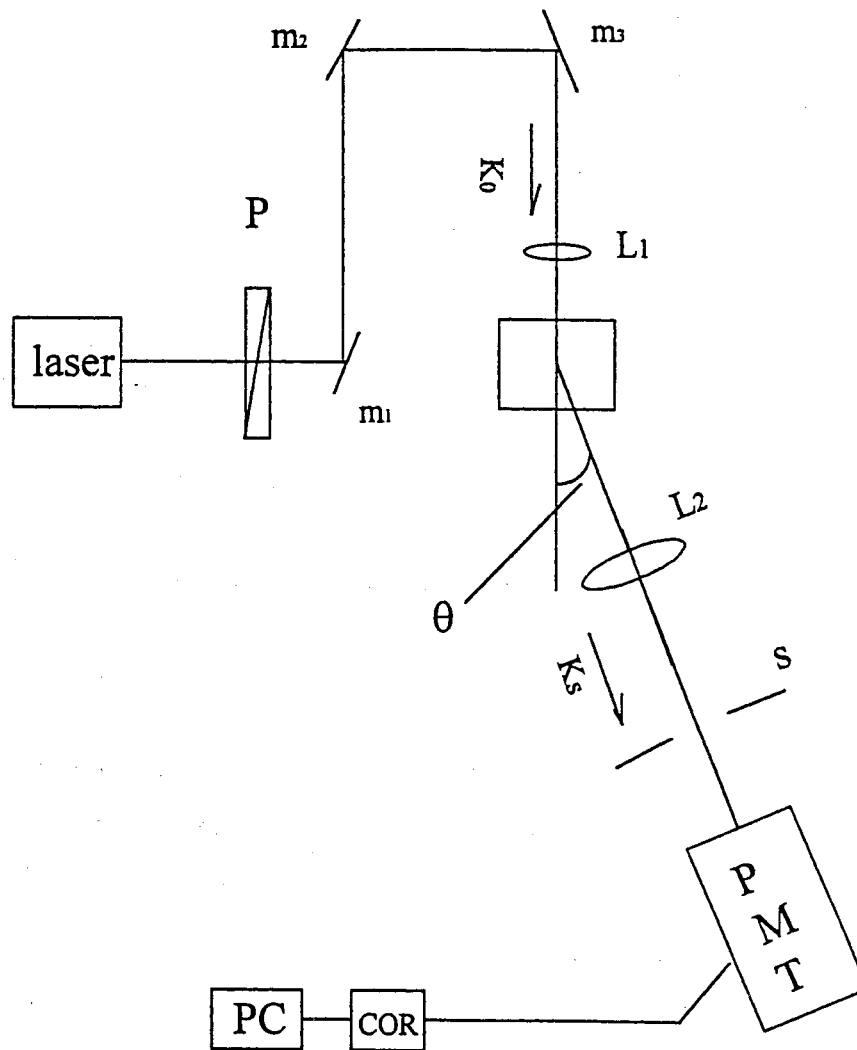$$h(R) = \frac{2(N - n)}{N(N - 1)} \simeq (2/N)(1 - n/N) = (2/L)(1 - R/L). \qquad (56)$$

Figure 10. Schematic diagram of HCS setup (vertical beam orientation).

Here we have assumed that $N \gg 1$ and that the particles are uniformly distributed in a quasi-one-dimensional scattering volume. Furthermore, the time average $< \cos[\mathbf{q} \cdot \delta\mathbf{v}(\mathbf{R}, t')t] >_{t'}$ can be replaced by an ensemble average, and Eq. (55) becomes

$$g(t) = 1 + \int_0^L dR\, h(R) \int_{-\infty}^{+\infty} d\left[\delta v_q(R)\right] P[\delta v_q(R)] \cos[\mathbf{q} \cdot \delta\mathbf{v}(\mathbf{R})t], \qquad (57)$$

where $\delta v_q(R)$ is the component of $\delta\mathbf{v}(\mathbf{R})$ along the direction of q, and $P[\delta v_q(R)]$ is the probability density function of $\delta v_q(R)$. When $P[\delta v_q(R)]$ has a scaling form

$$P[\delta v_q(R)] = u(R)^{-1} Q[\delta v_q(R)/u(R)], \qquad (58)$$

with $u(R)$ being a characteristic scaling velocity and $Q[\delta v_q(R)/u(R)]$ a homogeneous function, Eq. (57) becomes

$$g[qtu(L)] = 1 + \int_0^L dR\, h(R)\, F[qtu(R)]. \qquad (59)$$

In the above, $F[qtu(R)]$ is the Fourier cosine transform of $Q[\delta v_q(R)/u(R)]$.

Measurement Of Local Velocity Fluctuations

To overcome the difficulties in measuring the local velocity in convective turbulence, a new scattering method [36], named incoherent cross-correlation spectroscopy (ICS), is developed. This method measures the frequency spectrum of the scattering amplitude fluctuations, but not the rapid phase fluctuations caused by the relative Doppler shifts of the scattering particles. It has advantages of high spatial resolution, fast temporal response, and ease of use.

Figs. 11 and 12 show the setups for ICS. When comparing ICS with HCS, one finds two major differences in the set-up. First, the incident beam for ICS consisted of two colors, which was produced by an argon-ion laser (Coherent Innova-304) under the multiline operation with a wavelength range from 458.0 to 514.5 nm. Second, two photomultipliers, $PM1$ and $PM2$, were used to record the blue and the green lights, respectively, and they were mounted at right angles in a cubic box. A beam-splitter BS, which had a reflection-to-transmission ratio of 50/50, was placed at the center of the box, and it split the incoming light into the two
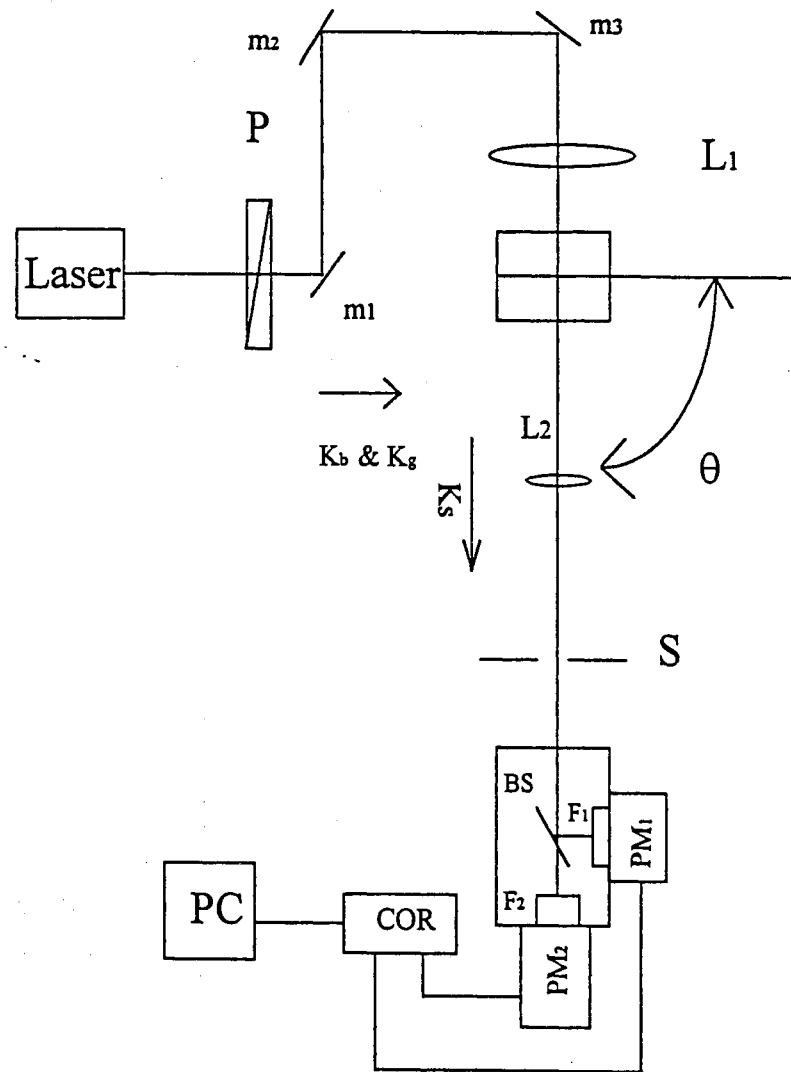
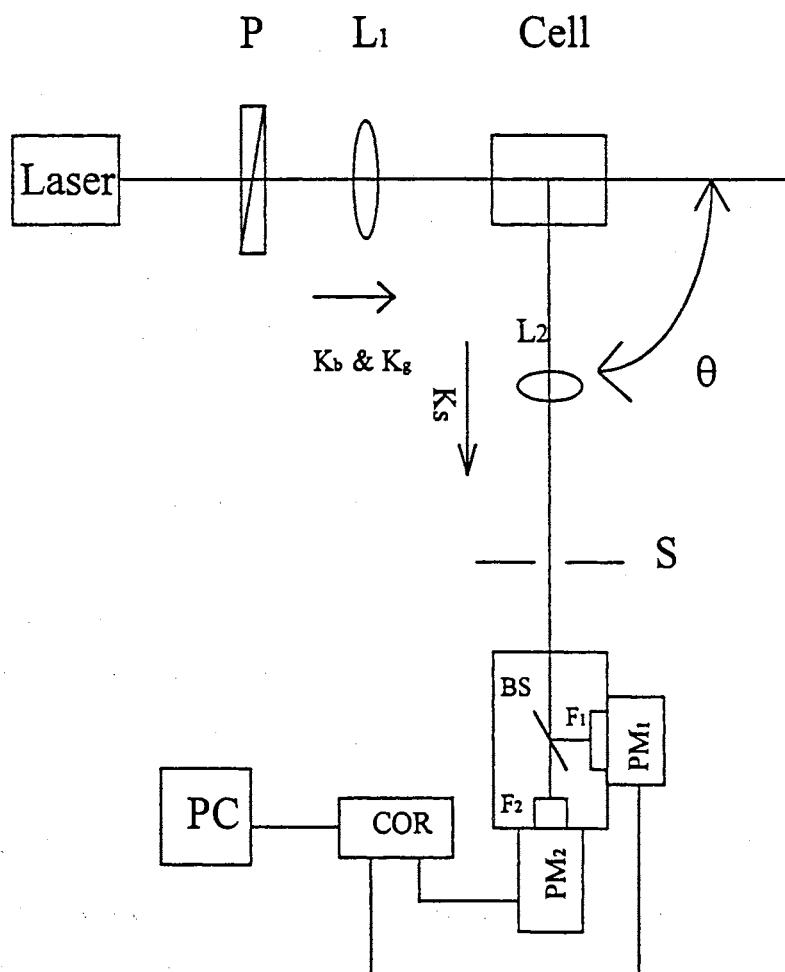Figure 11. Schematic diagram of ICS setup (vertical beam orientation).

Figure 12. Schematic diagram of ICS setup (horizontal beam orientation).

photomultipliers. Two interference filters ($F1$ and $F2$) were mounted in front of the photomultipliers, separately, and their band width was 1 nm. The spectral line for $F1$ was 488 nm, and that for $F2$ was 514.5 nm. The scattering volume viewed by the photomultipliers was a thin cylinder, whose length L is much larger than its waist radius σ. The intensity profile was measured using a translational stage, a pin hole of size $5\,\mu m$, and a photodiode. Figure 13 shows the measured intensity profile I(r) as a function of the radial distance r from the center of the laser beam. The solid curve is the fitted Gaussian form

$$I(r) = I_0 e^{-2(r/\sigma)^2},\tag{60}$$

with $\sigma = 48 \pm 3\,\mu m$ being the beam diameter, and I_0 being the light intensity at the center of the beam.

As discussed in the last section, when $\mathbf{q}_b \neq \mathbf{q}_g$, $g_{coh}(t) = 0$, and hence the measure $g_c(t) = 1 + b\,g_N(t)$. To have a larger signal-to-noise ratio for $g_N(t)$, the number of the particles in the scattering volume was controlled in the range $1 < N_{avg} < 100$. This is because $g_N(t)$ goes as $\frac{1}{N_{avg}}$. Large latex particles of $0.94\,\mu m$ in diameter were used in the measurements in order to have a better signal and each $g_c(t)$ was measured for more than 20 minutes. An ALV-5000 correlator was used to measured $g_c(t)$, and it is capable of measuring fluctuating signals with a signal-to-noise ratio as low as 0.1%.

Because of the fluid motion, the seed particles move in and out of the scattering volume and hence the particle numbers in the scattering volume changes with time. In this case, $g_N(t)$ can be rewritten as

$$g_N(t) = \frac{1}{N_{avg}} \frac{\int d^3r \int d^3r_0\, I(r)\, I(r_0)\, P(r - r_0, t)}{[\int d^3r\, I(r)]^2},\tag{61}$$

where $I(r)$ is the light intensity profile, and $P(r - r_0, t)$ is the probability density function for a particle to move from r_0 to r during time t. The function $P(r - r_0, t)$ characterizes the dynamics of the fluid motion. When the particles in the scattering volume have a uniform velocity v, the function $P(r - r_0, t)$ takes the form

$$P(r - r_0, t) = \delta[(r - r_0) - vt],\tag{62}$$
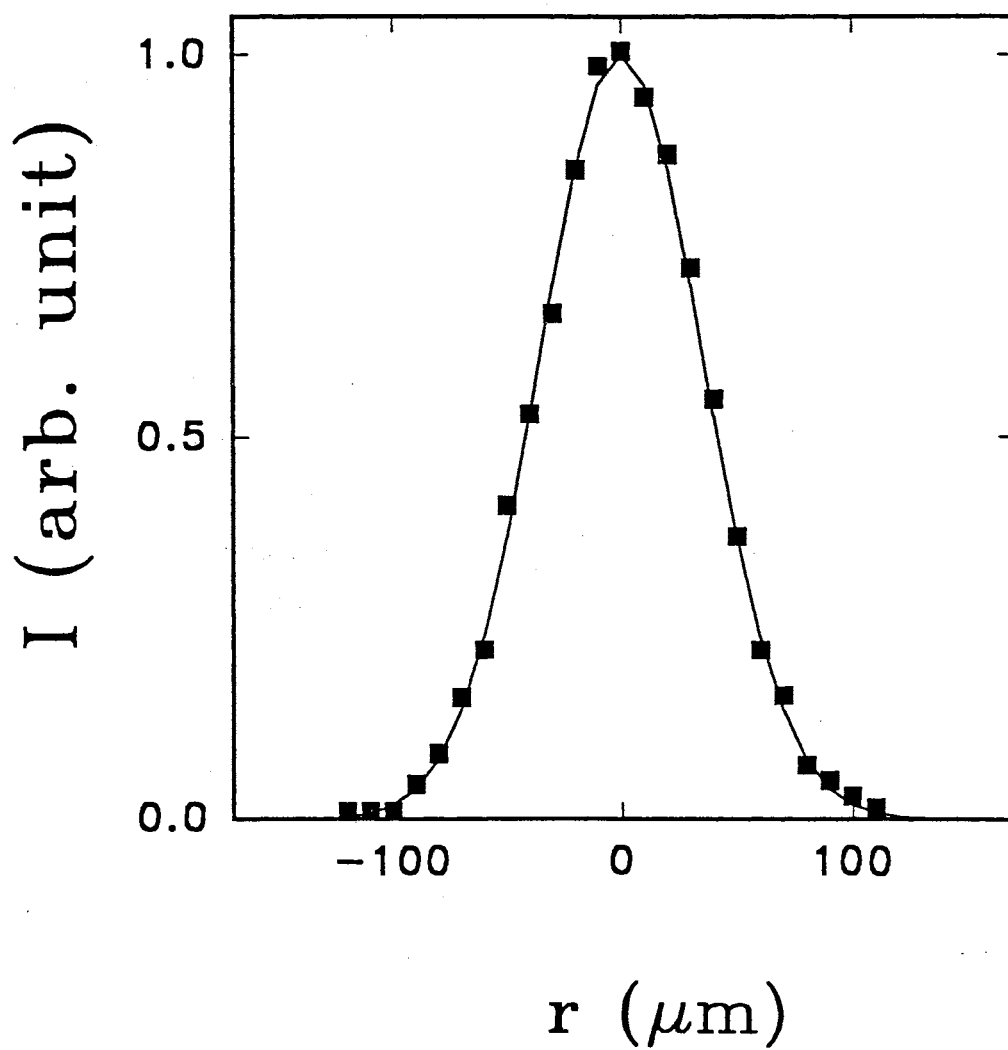
Figure 13. Measured intensity profile I(r) as a function of the radial distance r.

and then

$$g_N(t) = \frac{1}{N_{avg}} e^{-(vt/\sigma)^2}.$$

(63)

Because the time required for a particle to cross the laser beam is much shorter than the turbulent eddy turnover time t_L, Eq. (63) can also be applied to turbulent flow, as long as the local velocity v is averaged over its probability density function $P(v)$. In this case, Eq. (63) becomes

$$g_N(t) = \frac{1}{N_{avg}} \int_{-\infty}^{+\infty} dv_i \int_{-\infty}^{+\infty} dv_j \, P_2(v_i, v_j) \, e^{-(v_i^2 + v_j^2)t^2/\sigma^2},$$

(64)

where $P_2(v_i, v_j)$ is the probability density function for the velocity components v_i and v_j in two different directions, both orthogonal to the incident laser beam. Because of the radial symmetry of the laser beam, $g_N(t)$ is only sensitive to $v_i^2 + v_j^2$. This feature is particularly useful in studying the convective flow in the central region, where the mean velocity is zero and thus velocity fluctuations can be directly measured. Velocity components in different directions can be measured by changing the incident direction of the laser beam.

CHAPTER IV

EXPERIMENTAL RESULTS

In this chapter, we present our velocity measurements in turbulent convection. The first section is devoted to the measurements of the velocity difference $u(l)$ at various length scales. The second section discusses the local velocity measurements at the center of the convection cell. The third section presents the results of the heat transport and the local velocity measurements in a convection cell whose upper and lower plates are made of "rough" surfaces.

Velocity Difference At Various Scales

A unique feature of convective turbulence is its interaction with the gravitational field at various length scales. Temperature is not a passive scalar in the system. This is absent in the normal barotropic turbulence such as that in a pipe flow. According to the Kolmogorov theory [13] of fully developed barotropic turbulence, turbulent kinetic energy is continuously transferred from the largest eddies of size l_0 to eddies of smaller sizes, until it dissipates when the size of the eddies becomes comparable to the viscous dissipation length $l_{\min}$. In the inertial range, $l_{\min} \ll l \ll l_0$, the energy cascades at a constant rate ε with negligible dissipation. As a consequence of the argument, the velocity difference $\delta v(l, t)$ is expected to be scale invariant [8], and its probability density function $P(\delta v, l)$ has a homogeneous form

$$P(\delta v, l) = Q[\delta v / u(l)] / u(l). \tag{65}$$

With a simple dimensional argument [8][13], one can show that the scaling velocity $u(l) \sim (\varepsilon l)^{\frac{1}{3}}$ (for more details, also see discussion in Chapter II). For thermal convective turbulence, on the other hand, velocity fluctuations produce temperature

41

fluctuations of various sizes, and eddies of different sizes can exchange different amounts of energy with the gravitational field. Therefore, the energy cascade rate ε becomes l dependent, which will be responsible for the departure from the Kolmogorov scaling. It has been shown [18][22] that for convective turbulence, $u(l) \sim l^{3/5}$. Since the high-Ra convection provides an interesting variation of turbulence, direct measurement of the new exponent becomes fundamentally important in testing the general scaling argument for the description of turbulence.

Our experiment is carried out using both the horizontal beam setup and vertical beam setup, as described in Chapter III. The technique of photon-correlation homodyne spectroscopy (HCS) [3] is utilized to probe the instantaneous velocity difference $\delta v(l, t)$. With the HCS scheme, small seed particles in the fluid scatter light and follow the local flow. A photo-detector records the scattered light intensity $I(t)$, which fluctuates due to the motion of the flowing particles. The output of the detector is therefore modulated at frequencies equal to *differences* in Doppler shifts of all particle pairs in the scattering volume. The intensity autocorrelation function [3]

$$g(t) = \frac{< I(t' + t)\, I(t') >}{< I >^2} = 1 + b\, G(q, t, l), \qquad (66)$$

is measured as a function of the delay time t for different values of q and l. In the above, b is an instrumental constant which is chosen so that

$$G(t = 0) = 1. \qquad (67)$$

When the PDF $P(\delta v, l)$ has the homogeneous form shown in Eq. (65) as we have derived in Chapter III, the function $G(q, t, l)$ becomes [33]

$$G\,[qtu(L)] = \int_0^L dl'\, h(l')\, F[qtv(l')], \qquad (68)$$

where $h(l')$ is the number faction of particle pairs separated by a distance l' in the thin scattering volume of length L and $F[qtv(l')]$ is the Fourier cosins transform of $Q[V/u(l')]$. The HCS technique has been used previously to study turbulent flows in a pipe and in a square tunnel [33][34].

To characterize the decaying function $G(q, t, L)$, which does not necessarily behave like an exponential function, a decay rate $\Gamma(q, L)$ is defined as

$$\Gamma^{-1}(q, L) = \int_0^\infty dt\, G(q, t, L). \tag{69}$$

This definition of $\Gamma(q, L)$ emphasizes the initial decay of $G(q, t, L)$ governed by L. With a simple dimensional argument one can show that [33]

$$\Gamma(q, L) \simeq q\, u(L). \tag{70}$$

Thousands of correlation functions have been measured as a function of L and Ra. In the absence of convection ($Ra = 0$), $G(q, t, L)$ still decays because of the Brownian motion of the seed particles. The Brownian motion contributes a factor $\exp(-2D_B\, q^2 t)$ to $G(q, t, L)$, where D_B is the diffusion constant of the seed particles [3]. The Brownian decay rate $2D_B q^2$ has been subtracted from the measured $\Gamma(q, L)$. This correction is especially important for the low-Ra data, because the flow-induced decay rate in this case is comparable to the Brownian decay rate.

The measured $G(q, t, L)$ is found to be of scaling form $G(\kappa)$ as shown in Eq. (68), with

$$\kappa = \Gamma(q, L)t \simeq q\, u(L)\, t. \tag{71}$$

To verify the scaling form for $G(\kappa)$, we superimpose Log-Log plots of the measured $G(q, t, L)$ for different L by sliding them horizontally with respect to each other. The decay time $\Gamma^{-1}(q, L)$ defined above quantitatively characterizes the amount of the horizontal translation that is required to bring the correlation functions into coincidence. Figure 14 shows a typical Log-Log plot of $G(\kappa)$ as a function of κ for various values of L and Ra. The functions coincide well with each other. Additional measurements have been conducted to verify the linear q-dependence of the decay rate $\Gamma(q, L)$. With fixed values of L and Ra, we measured $G(q, t, L)$ for different scattering angles, ranging from $30°$ to $110°$. Figure 15 shows the measured $\Gamma(q, L)$ vs. q. The straight fitting line in Figure 15 is the fitting function $0.15 + 5 \times 10^{-4} q$. As shown in Eq. (68), a scaling $G[qu(l)t)]$ implies that the probability density

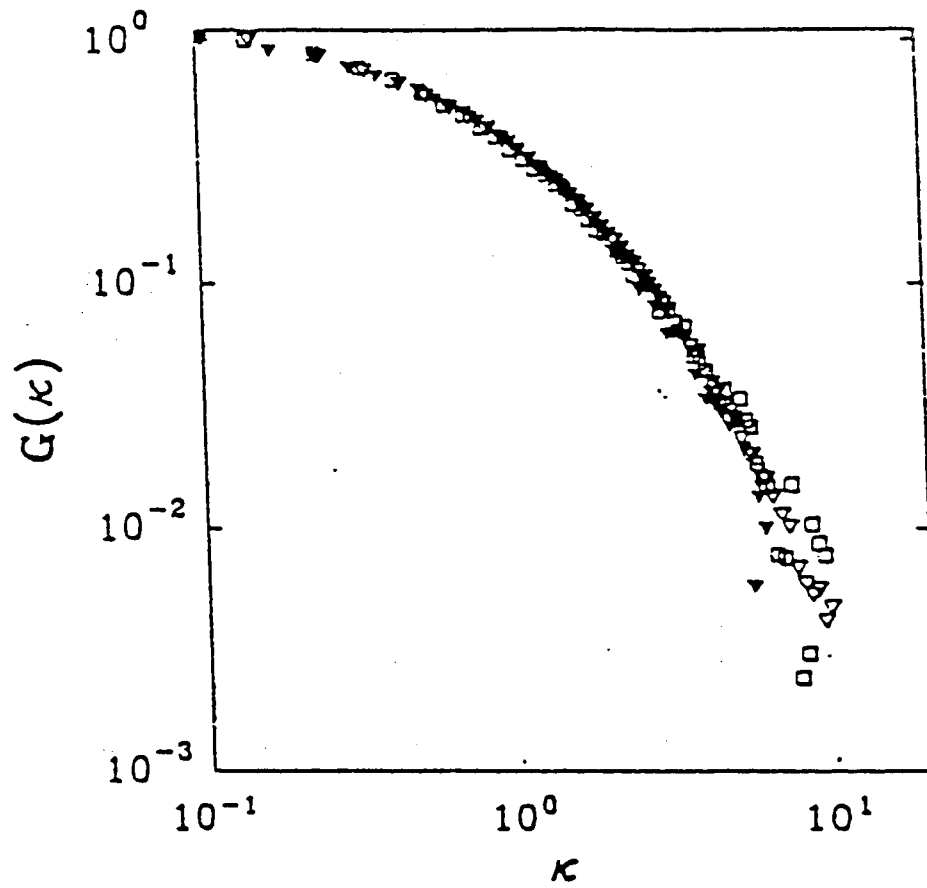Figure 14. The scaling correlation function. The experimental conditions are $L = 4.1mm$, $Ra = 9.1 \times 10^9$ (solid triangles); $L = 6.8mm$, $Ra = 9.1 \times 10^9$ (open aquares); and $L = 13.5mm$, $Ra = 3.4 \times 10^9$ (open triangles).
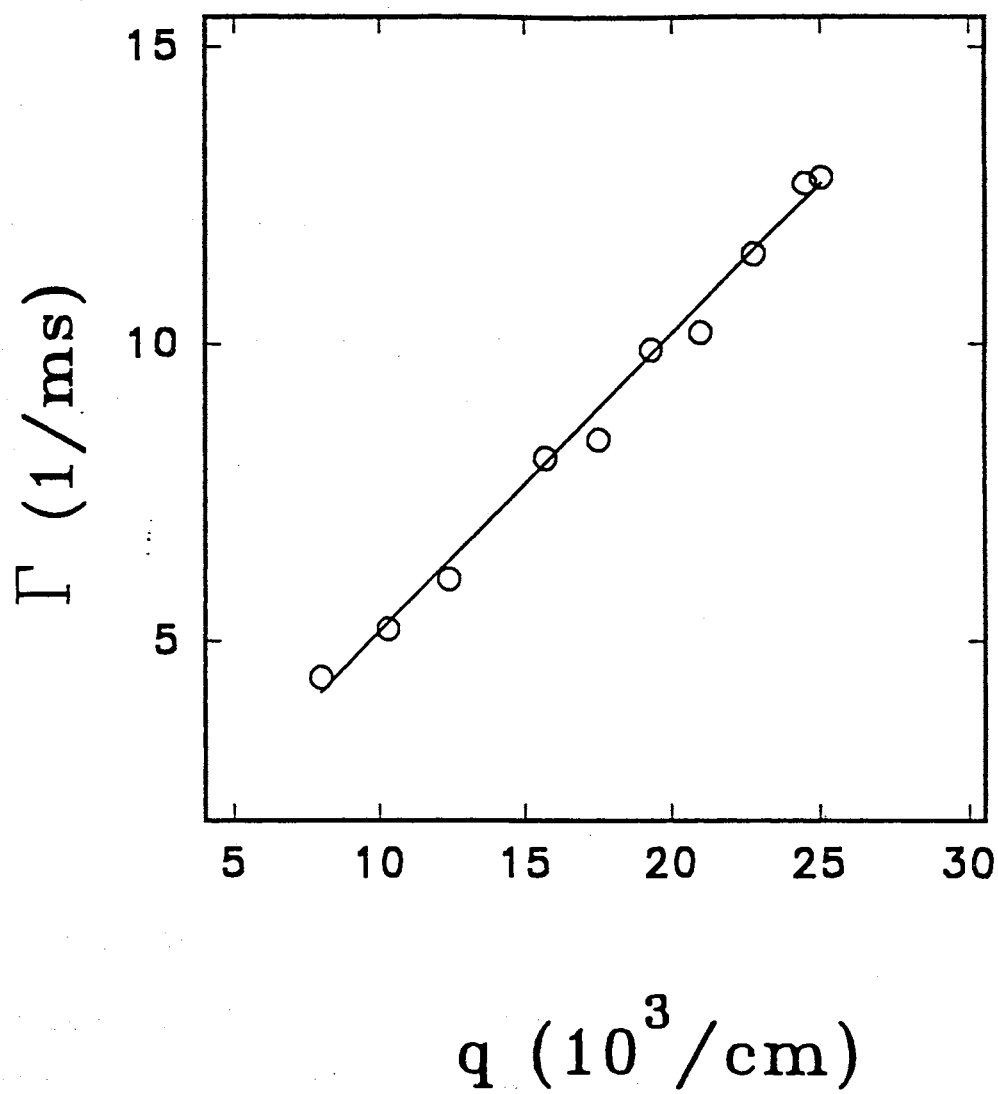
Figure 15. The measured decay rate of the correlation function as a function of the scattering vector q. The experimental conditions are $Ra = 5.7 \times 10^{10}$, $L = 8.8mm$.

function $P(\delta v, l)$ has the form shown in Eq. (65). Our data thus suggests that the functional form of $P(\delta v, l)$ and, hence, the turbulent structure are invariant in Ra, and the statistical properties of $\delta v(l, t)$ over varying length scales become identical under an appropriate scaling of velocities.

The scale dependence of the scaling velocity is examined by measuring the L-dependence of $\Gamma(q, L)$. Figure 16 shows the measured $\Gamma(q, L)$ as a function of L at three different values of Ra, when the laser beam is shone through the cell horizontally. In this case, the direction of the velocity difference is perpendicular to the direction of the gravity. Figure 17 shows the measured $\Gamma(q, L)$ as a function of L at three different values of Ra, when the laser beam is in the vertical direction. The velocity difference measured in this beam orientation has a component parallel to the direction of the gravity There are several important features in these two plots. First, the decay rate $\Gamma(q, L)$ as a function of L obeys a power law

$$\Gamma(L) \sim L^{\xi}, \tag{72}$$

and thus,

$$u(L) \sim L^{\xi}. \tag{73}$$

From the straight-line segment (solid lines in Figs. 16 and 17), one finds the exponent

$$\xi = 0.60^{+0.02}_{-0.04}, \tag{74}$$

for both the vertical and horizontal velocity differences. The power-law behavior of $\Gamma(q, L)$ is found when $2 \times 10^7 \leq Ra \leq 10^{11}$. Our experiment, therefore, directly confirms the theoretical prediction [18][22] that $\xi = \frac{3}{5}$. The exponent ξ was also inferred from a temperature measurement by Wu et $al.$ [39].

Second, the velocity differences $u(L, t)$ at the center of the convection cell are isotropic. Figure 18 compares the measured $\Gamma(q, L)$ and hence $u(L)$ for the vertical beam (solid circles) with that for the horizontal beam (open circles) at $Ra = 1.1 \times 10^{11}$. Figure 18 shows that the components of the relative velocity in different directions not only obey the same power law but also have the same
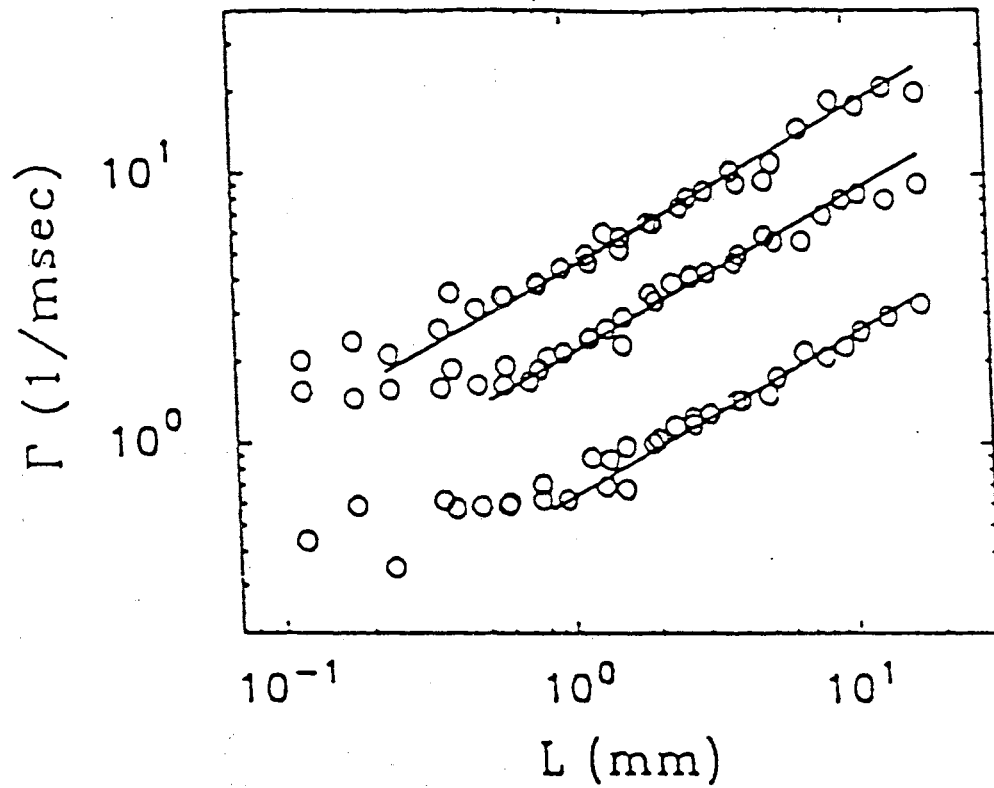
Figure 16. Variations of the decay rate $\Gamma(L)$ with the length L (horizontal beam
orientation) measured at $Ra = 9.1 \times 10^9$ (top curve), $Ra = 2.2 \times 10^9$
(middle curve), and $Ra = 3.7 \times 10^8$ (botttom curve). The solid
lines are power-law fits: $4.47L^{0.6}$ [1/ms] (top line), $2.14L^{0.6}$ [1/ms]
(moddle line), and $0.63L^{0.6}$ [1/ms] (bottom line).
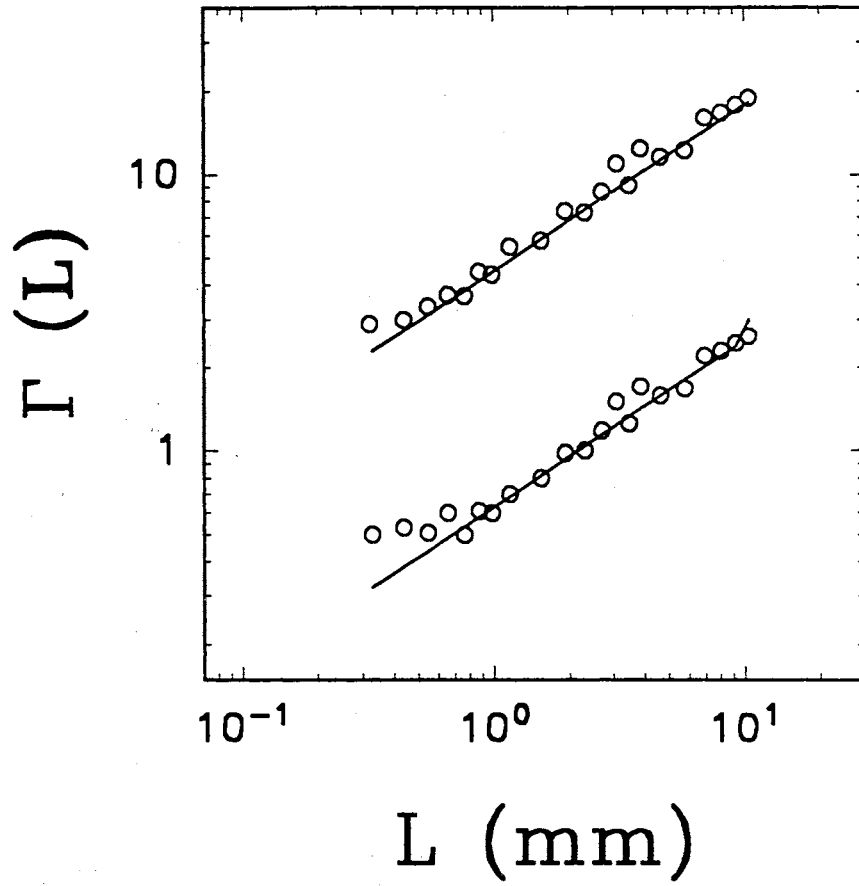
Figure 17. Variations of the decay rate $\Gamma(L)$ with the length L (vertical beam orientation) measured at $Ra = 1.0 \times 10^{10}$ (top curve), and $Ra = 3.7 \times 10^8$ (botttom curve). The solid lines are power-law fits: $4.5L^{0.6}$ [1/ms] (top line), and $0.63L^{0.6}$ [1/ms] (bottom line).
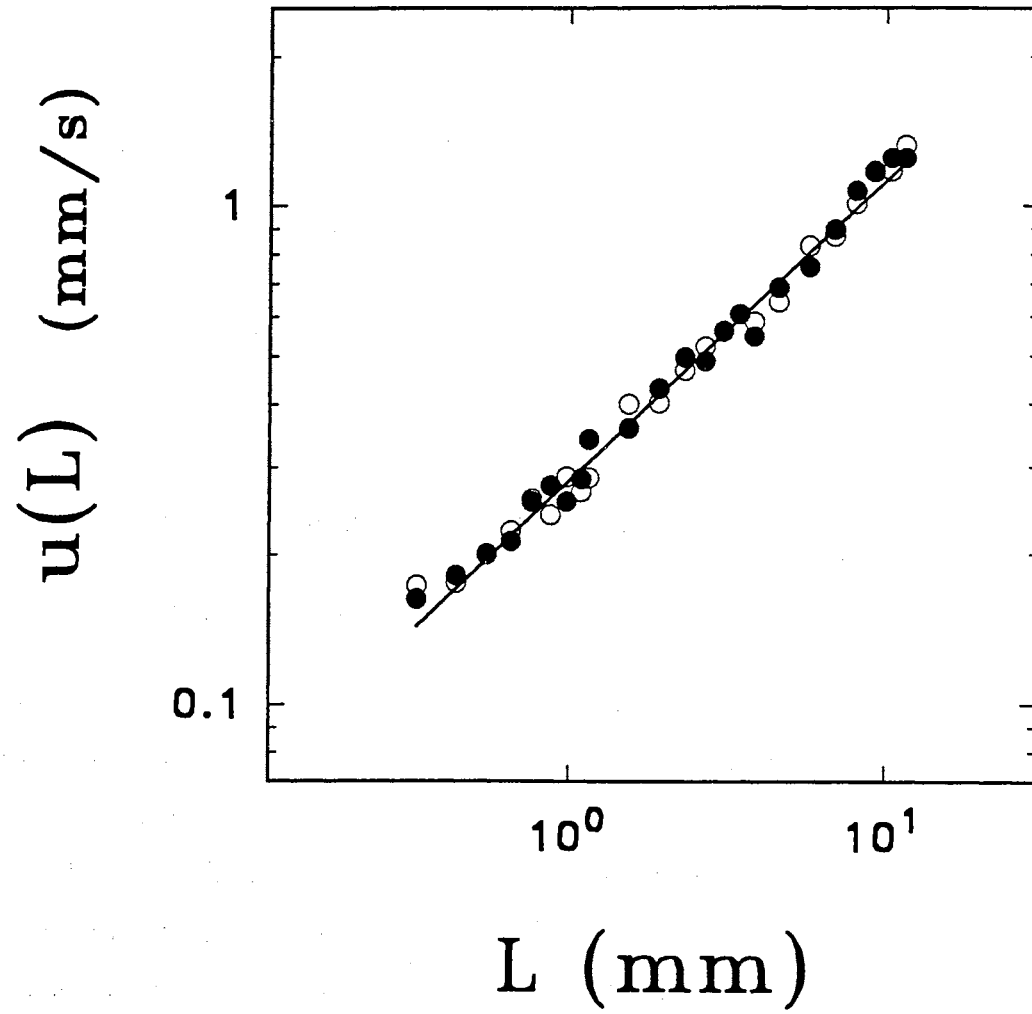
Figure 18. Measured velocity differences in vertical direction (open circles) and horizontal direction (solid circles) at $Ra = 1.1 \times 10^{11}$. The solid line is the power-law fit: $u(L) = 0.274L^{0.6}$.

magnitude when the control parameter, Ra, is the same. This suggests that the small-scale relative velocity fluctuations in turbulent convection are isotropic.

The third feature in Figs. 16 and 17 is that at a fixed L, the measured $\Gamma(q, L)$ [or equivalently $u(L)$] is also a function of Ra. In Figure 19a, the dimensionless velocity (Reynolds number), $Re(L) = h\,u(L)/\nu = h\Gamma(L)/q\nu$, is plotted as a function of Ra for two different values of L. The measured $Re(L)$ as a function of Ra is well described by the power law (solid lines)

$$Re(L) \sim Ra^{0.67}. \tag{75}$$

The uncertainty for the exponent is ± 0.03. Combining Figs. 16, 17, and 19, we have

$$Re(L) \sim Ra^{0.67} L^{3/5}. \tag{76}$$

This result appears to be different from the theoretical prediction [18] that

$$Re(L) \simeq (L/h)^{3/5} Ra^{1/2}. \tag{77}$$

One possible reason for this deviation from the predicted scaling exponent in Ra is the anisotropic nature of convective turbulence at length scales comparable to the size of the cell h. Fluctuations of the velocity difference $\delta v(l, t)$, between two points separated by $l \simeq h$, in the direction parallel to the gravity are certainly different from those in the perpendicular direction. Unlike the situation in the central region where the flow is isotropic, there is enough turbulent mixing near the sidewalls and the upper and lower plates. The prediction in Eq. (77), on the other hand, is obtained by assuming the velocity fluctuations are isotropic when $l \simeq h$. Put in another way, the local Rayleigh number $Ra(L)$ should be used as a scaling variable rather than the global Rayleigh number Ra. This argument can explain the observation that the h-dependence of the measured $Re(L)$ is also different from the theoretical prediction. Figure 19 shows the measured $Re(L)$ as a function of Ra at $L = 13.5\,mm$ in the $h = 6.6\,cm$ cell (open circles). The solid line in the plot is the power-law fit $Re(L) \sim Ra^{0.67}$. The dashed line shows the extrapolation of the measured $Re(L)$ in the $h = 20\,cm$ cell with the predicted $h^{-3/5}$

Figure 19. The measured Reynolds number Re(L) as a function of Ra. (a)
$L = 13.5mm$ (solid circles) and $L = 5.4mm$ (open circles) in
the $h = 20cm$ cell. The solid line are the power-law fits by
$Re(L) \sim Ra^{0.67}$. (b) $L = 13.5mm$ (open circles) in the cell with
$h = 6.6cm$. The solid line is the power-law fit by $Re(L) \sim Ra^{0.67}$.
The dashed line shows the extrapolation of the measured Re(L) in
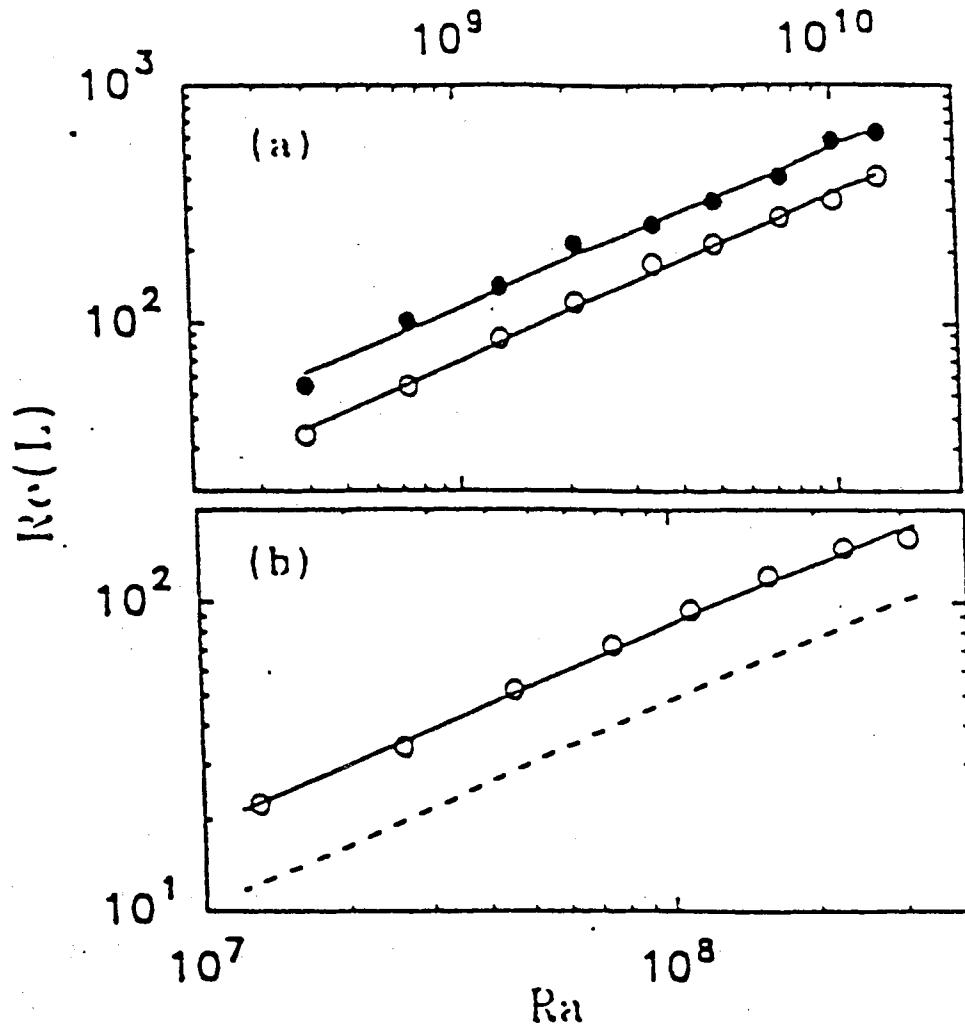the $h = 20cm$ cell with the $h^{-3/5}$ correction.

correction. Figure 19 also shows that $Re(L)$ is larger for smaller values of h when the other experimental conditions are kept unchanged. However, the data fails to show the predicted $h^{-3/5}$ dependence.

Another feature in Figs. 16 and 17 is that there is a cutoff length l_c, below which $\Gamma(q, L)$ levels off. It is seen that the cutoff length l_c decreases as Ra is increased. The measured l_c as a function of Ra is shown in Figure 20 (solid circles). The result can be described by the power law (lower solid line)

$$l_c = 34.3 Ra^{-\varphi} cm.$$

The exponent $\varphi = 0.3 \pm 0.03$, which agrees with the theoretical prediction [18]

$$l_c \sim Ra^{-5/16}.$$

The scatter in the data is due to the uncertainty in determining l_c from the plot of $\Gamma(L)$ vs L. Procaccia and Zeitak [22] have proposed that there may be a length scale,

$$l_c \sim Ra^{-3/28},$$

below which a crossover to Kolmogorov exponents is expected. However, such a length scale is not observed in our measurements of $\Gamma(q, L)$. This finding supports L'vov's argument that in high-Ra convective turbulence the entropy flux at various length scales is constant [17][18].

We now address an important issue concerned with the relationship between coherent structures and the velocity scaling. It has been found [29][40] that the thermal plume is one of the two main coherent structures in the convective turbulence. The thermal plumes consist of a column of buoyant fluid emanating from the boundary layer and culminating in a cap, and become free plumes not connected to the boundary layers when they move into the central region of the cell. Because they are generated from the boundary layers, the smallest size of these coherent structures (the diameter of the thermal plumes, see Fig. 1 of Ref. [40]) is naturally controlled by the thermal boundary layer thickness δ. In Figure 20 we plot δ (open triangles), which is obtained from the measured Nusselt number Nu,
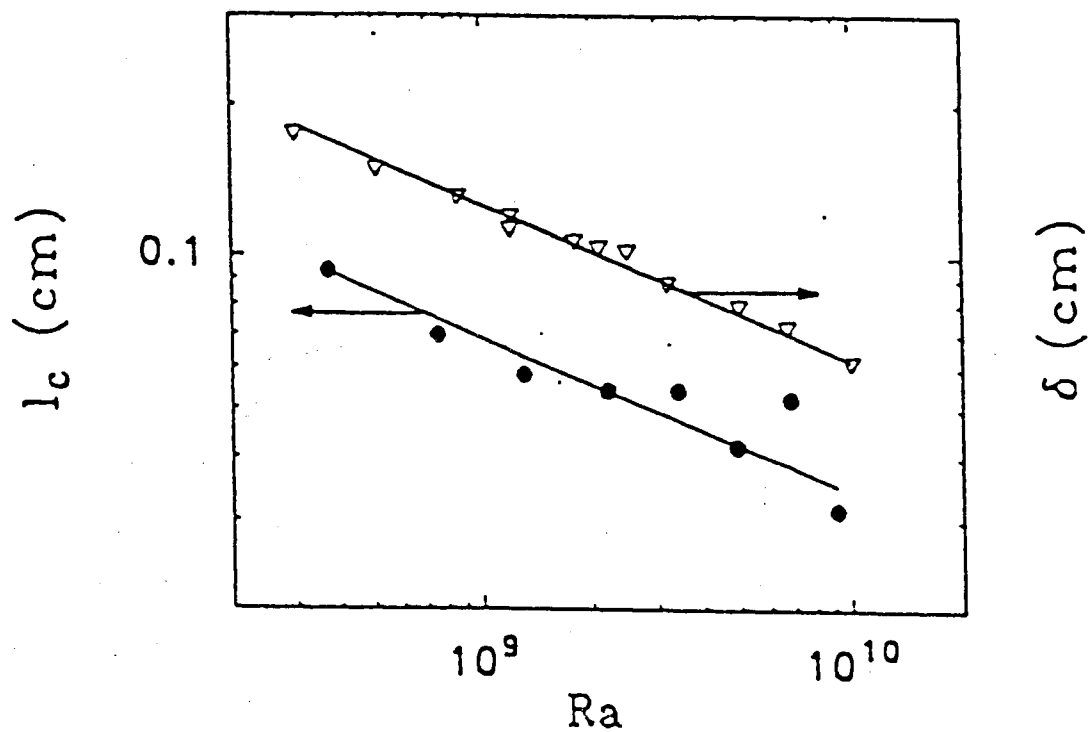
Figure 20. Variations of the cutoff length (solid circles) and thermal boundary thickness (open triangles) as a function of Ra. The upper solid line is a power-law fit $63.0 Ra^{-0.3}$ [cm], and the lower solid line is $34.3 Ra^{-0.3}$ [cm].

using the well tested relation $\delta = h/(2Nu)$. The data are well described by the power law

$$\delta = 63.0 Ra^{-0.3} \, cm,$$

when $5 \times 10^7 \leq Ra \leq 10^{10}$. It turns out that the value of our δ is very close to the value measured directly from the temperature profile in a similar convection cell [40]. It is seen from Figure 20 that the two length scales, l_c and δ, have similar power-law behavior. The values of the two exponents are the same within our experimental uncertainties. The numerical values of the two length scales only differ by a factor of 2.

As shown in Figs. 16 and 17, the measured $\Gamma(q, L)$ becomes L−independent below l_c. This is an interesting phenomenon. New measurements are in progress to investigate the velocity field at the scale below l_c [32]. It should be mentioned that below l_c the typical decay time of $G(q, t, L)$ becomes close to the Brownian diffusion time of the seed particles, and therefore the velocity signal is very small. The leveling-off behavior might be caused by the interaction between the convective flow and the Brownian motion [9]. I think it is plausible that the measured cutoff length l_c in the velocity scaling is determined by the thermal boundary layer thickness, which is the smallest scale for the coherent structures in the core region of turbulent convection.

Local Velocity Fluctuations In Turbulent Convection

Figs. 11 and 12 in Chapter III show the experimental setup for the measurements of the local velocity at the center region of the cell. The newly developed technique of incoherent cross-correlation spectroscopy (ICS) [36] was utilized to probe the local velocity v and its probability density function (PDF) $P(v)$. Previous temperature measurements have revealed two distinct turbulent states in convection: soft turbulence when $Ra < 10^8$ and hard turbulence for $Ra > 10^8$ [12]. The Rayleigh number range of our velocity measurements covered the upper end of the soft turbulence region and three decades of the hard turbulence region. Velocity components in different directions were measured in both turbulent states.

As we have already discussed in Chapter III, with the ICS scheme, one uses two photodetectors to record the scattering intensities of the blue and green lights, $I_b(t)$ and $I_g(t)$, respectively. The output signals then are fed to an ALV-5000 correlator, whose output gives the intensity cross-correlation

$$g_c(t) = \frac{< I_b(t' + t) \, I_g(t') >}{< I_b >< I_g >} = 1 + bG_c(t),\qquad(78)$$

where b (≤ 1) is an instrumental constant. Because there is no phase coherence between $I_b(t)$ and $I_g(t)$, $g_c(t)$ is only sensitive to the scattering amplitude fluctuations produced by the seed particles moving in and out of the laser beam. Therefore, the $G_c(t)$ measures the particle number fluctuation in the scattering volume. When the seed particles have a uniform velocity v, $G_c(t)$ in Eq. (78) takes the form [36]

$$G_c(t) = \frac{1}{N_{avg}} \, e^{-(vt/\sigma)^2}.\qquad(79)$$

where N_{Avg} is the average number of the particles in the scatting volume. For turbulent flows $G_c(t)$ becomes

$$G_c(t) = \frac{1}{N_{avg}} \int_{-\infty}^{+\infty} dv_i \int_{-\infty}^{+\infty} dv_j P_2(v_i,v_j) e^{-(v_i^2+v_j^2)t^2/\sigma^2},\qquad(80)$$

where $P_2(v_i,v_j)$ is the PDF for the velocity components v_i and v_j in two different directions, both orthogonal to the incident laser beam. The decay time for $G_c(t)$ is the transit time for a particle to cross the laser beam, whose intensity profile is of Gaussian form $I = I_0 \exp[-2(r/\sigma)^2]$, with r being the radial distance from the center of the beam. By changing the direction of the incident laser beam, one can measure different components of the local velocity. Because of the axial symmetry of the laser beam, $G_c(t)$ is only sensitive to $v_i^2 + v_j^2$. This feature is particularly useful in studying the convective flow in the central region, where the mean flow velocity is zero [2] and, thus, velocity fluctuations can be directly measured. Because the acceptance angle of the receiving optics is large enough, small amplitude beam wandering in the convecting fluid will not affect the measurement.

Figure 21 shows the measured $g_c(t)$ as a function of the delay time t at $Ra = 3.5 \times 10^{10}$. The measurement was made when the laser beam was horizontally
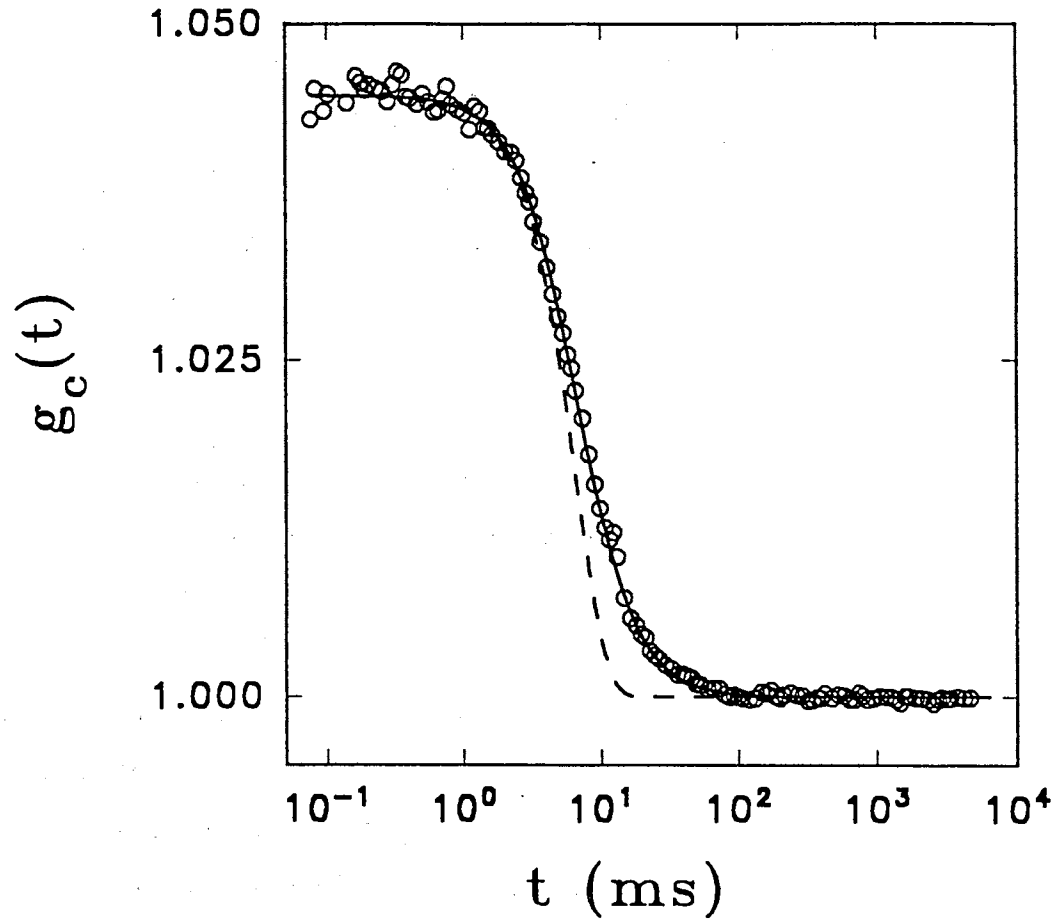
Figure 21. The measured cross-correlation function as a function of the delay time
t at $Ra = 3.5 \times 10^{10}$. The solid curve is a fit to $1 + a/(1 + (\Gamma t)^2)$ with
$a = 0.045$ and $\Gamma = 0.15 ms^{-1}$. The dashed curve shows a Gaussian
function $1 + a exp[-(\gamma t)^2]$.

shone through the center of the cell with the aspect Ratio $A = 0.5$. The data can be well fitted by the function

$$g_c(t) = 1 + \frac{a}{1 + (\Gamma t)^2},\tag{81}$$

with $a = 0.045$ and $\Gamma = 0.15\,ms^{-1}$ (the solid curve). The Lorentzian form of the measured $G_c(t)$ $[= g_c(t) - 1]$ differs substantially from the Gaussian function (the dashed curve) shown in Eq. (79), which has been measured in a laminar Poiseuille flow [36]. According to Eq. (80), the PDF, $P_2(v_i, v_j)$, can be obtained by a simple Laplace inversion of the measured $G_c(t)$. For a Lorentzian $G_c(t)$, we find the corresponding $P_2(v_i, v_j)$ is of the Gaussian form

$$P_2(v_i, v_j) = \frac{1}{v_0^2}\, e^{-(v_i^2 + v_j^2)/v_0^2},\tag{82}$$

where $v_0 = \Gamma \sigma$ is the rms velocity. To obtain Eq. (82), we have used the fact that velocity fluctuations in the central region are isotropic (see Figs. 24 and 25 below). Gaussian-like velocity PDF's have also been found in many barotropic turbulent flows [21].

The Lorentzian form of the measured $G_c(t)$ is found to remain unchanged when Ra is in the range between 10^8 and 10^{11}. In this Ra range only the decay rate Γ changes with Ra. Plots of $G_c(t)$ at different Ra can be brought into coincidence by scaling the time axis with Γ. Figure 22 shows typical $G_c(t)$ as a function of Γt for various values of Ra when the laser beam was shone horizontally through the cell center. Figure 23 shows typical $G_c(t)$ as a function of Γt when the laser beam was shone vertically through the center of the cell. Note that the two beam orientations actually probe different components of the local velocity. In the former case (horizontal beam) the velocity components in the vertical direction and in one of the horizontal directions are measured, whereas in the latter case (vertical beam) only the horizontal components of the local velocity are measured. It is seen from Figs. 22 and 23 that the measured $G_c(t)$'s in the hard turbulence regime superimpose with each other. Furthermore, the measured $G_c(t)$'s in two different beam orientations are found to have the same Lorentzian form. This suggests

Figure 22. The measured cross-correlation function as a function of Γt when the laser beam was horizontally shone through the cell center. The experimental conditions are (1) $Ra = 7.5 \times 10^{10}$ (solid circles); (2) $Ra = 2.3 \times 10^9$ (open squares); (3) $Ra = 4.6 \times 10^7$ (open circles); (4) $Ra = 1.4 \times 10^7$ (solid triangles).
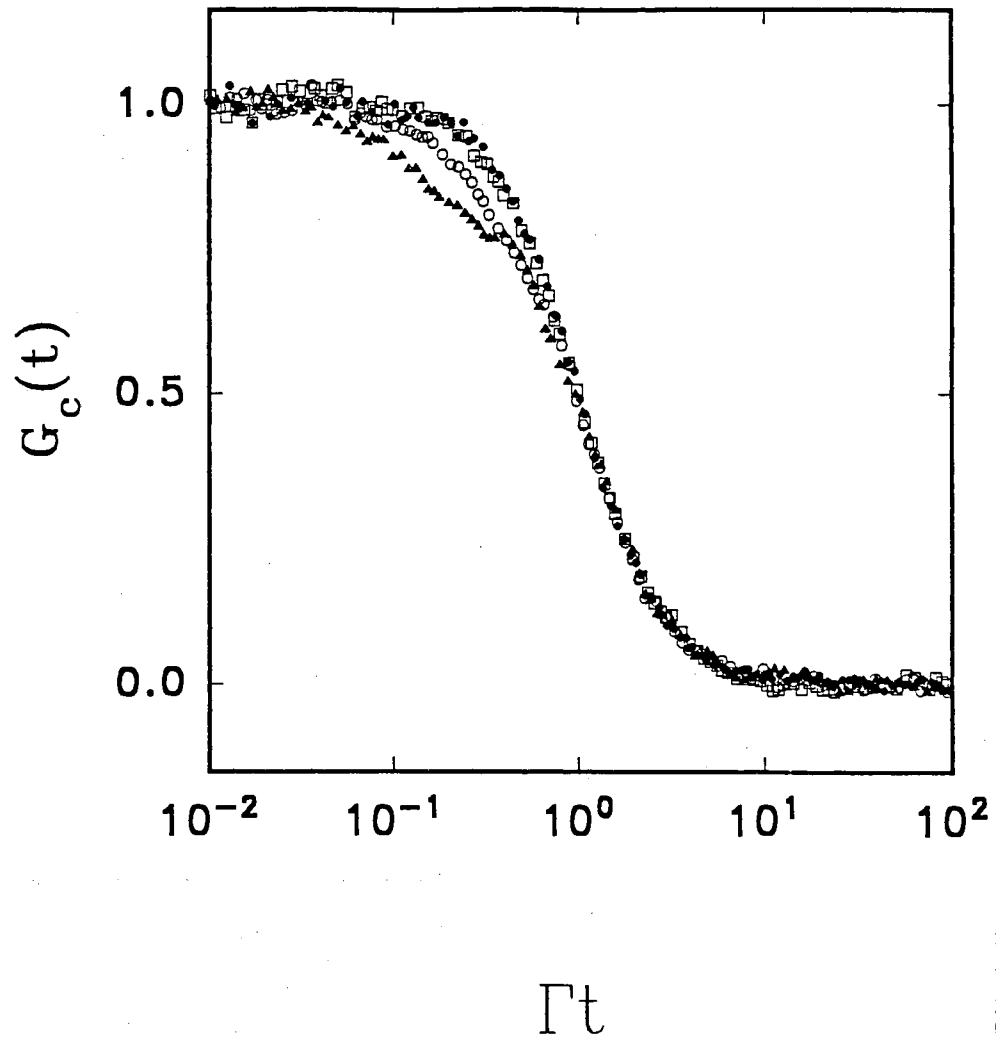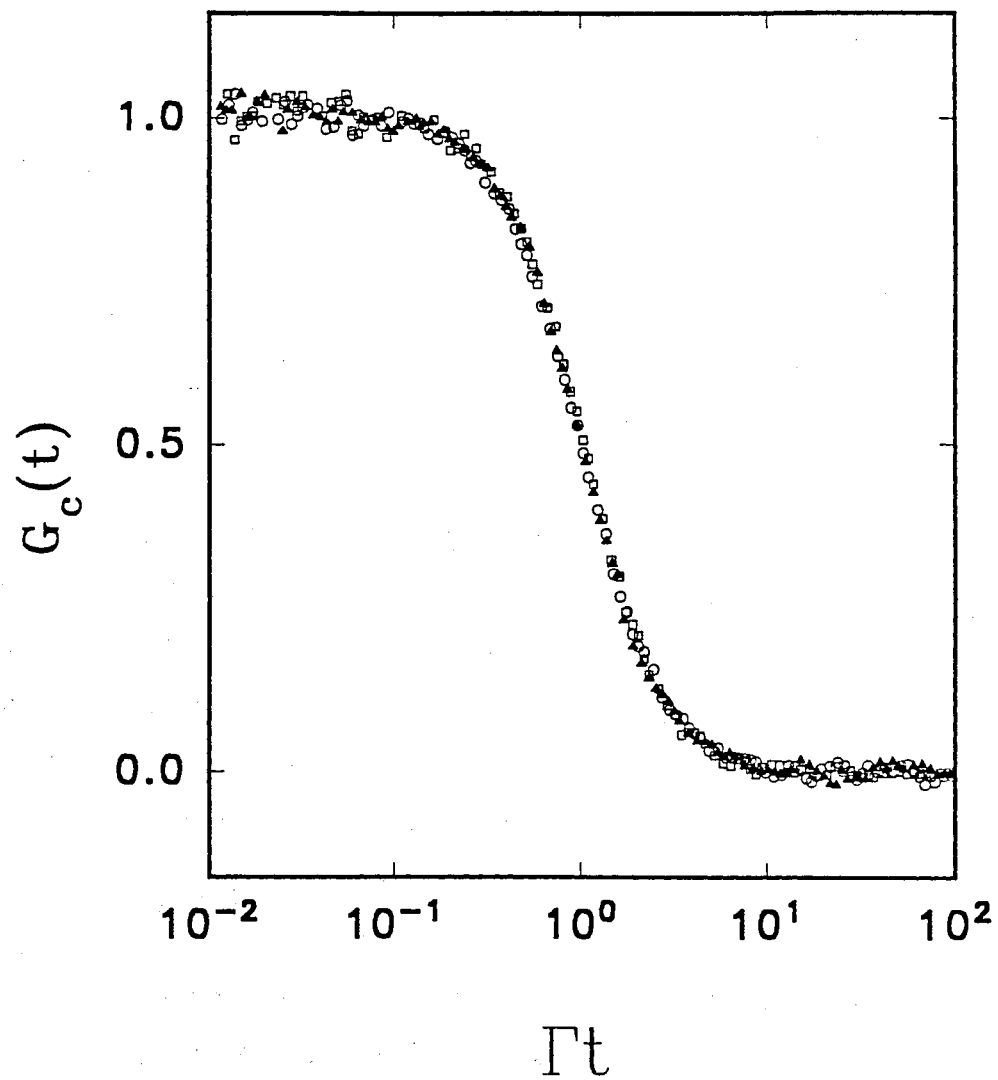
Figure 23. The measured cross-correlation function as a function of Γt when the laser beam was vertically shone through the cell center. The experimental conditions are (1) $Ra = 4.4 \times 10^{10}$ (open circles); (2) $Ra = 7.8 \times 10^8$ (solid triangles); (3) $Ra = 2.1 \times 10^7$ (open squares)

that the functional form of $P_2(v_i, v_j)$ and, hence, the turbulent structure in the hard turbulence regime are invariant with Ra. In mixing length theories, velocity fluctuations are often related to temperature fluctuations δT through the buoyancy effect [6]

$$v(t) = [\alpha g h \delta T t]^{1/2}. \qquad (83)$$

If this is true in a strict deterministic sense (i.e., hotter fluid moves faster), then the PDF for v would be the same as that for $\sqrt{\delta T}$. In fact, it is known that the PDF for $\sqrt{\delta T}$,

$$P(\sqrt{\delta T}) = 2\sqrt{\delta T}\, \tilde{P}(\delta T), \qquad (84)$$

is not a Gaussian function, because the measured PDF $\tilde{P}(\delta T)$ for δT is a simple exponential function [6][12]. Figs. 21, 22, and 23 thus imply that velocity fluctuations at small scales are not strongly influenced by the buoyancy.

With the measured σ and Γ, we now plot the rms velocity, $v_0 = \Gamma \sigma$, as a function of Ra. Figure 24 compares the measured v_0 for the vertical beam (open circles) with that for the horizontal beam (solid circles) at different Ra. The measurements were made in the cell with $A = 0.5$. It is found from Figs. 22, 23, and 24 that velocity fluctuations in the central region are isotropic. As shown in Figure 25, the measured v_0 is well described by the power law

$$v_0 = 2.2 \times 10^{-5} Ra^\epsilon \ (cm/s). \qquad (85)$$

The straight line is the fit with $\epsilon = 0.44 \pm 0.015$. If the Peclet number, $Pe = v_0 h / \kappa_d$, is chosen as a dimensionless velocity, we find from Figure 25 that

$$Pe = 0.30 Ra^{0.44}. \qquad (86)$$

Using mixing length ideas, Kraichnan [14] predicts $\epsilon = 4/9$, and recent scaling arguments [6][27] give $\epsilon = 3/7$. While we cannot resolve the small difference between the two predicted values of ϵ within the experimental uncertainties, the measured ϵ is certainly in good agreement with the theoretical predictions. A similar value of ϵ was also obtained in previous experiments [10][30], where the velocity data from different convection systems were compiled together. However, difficulties in

Figure 24. The measured local velocity fluctuations as a function of Ra for the vertical beam (open circles) and for the horizontal beam (solid circles) with $A = 1$.
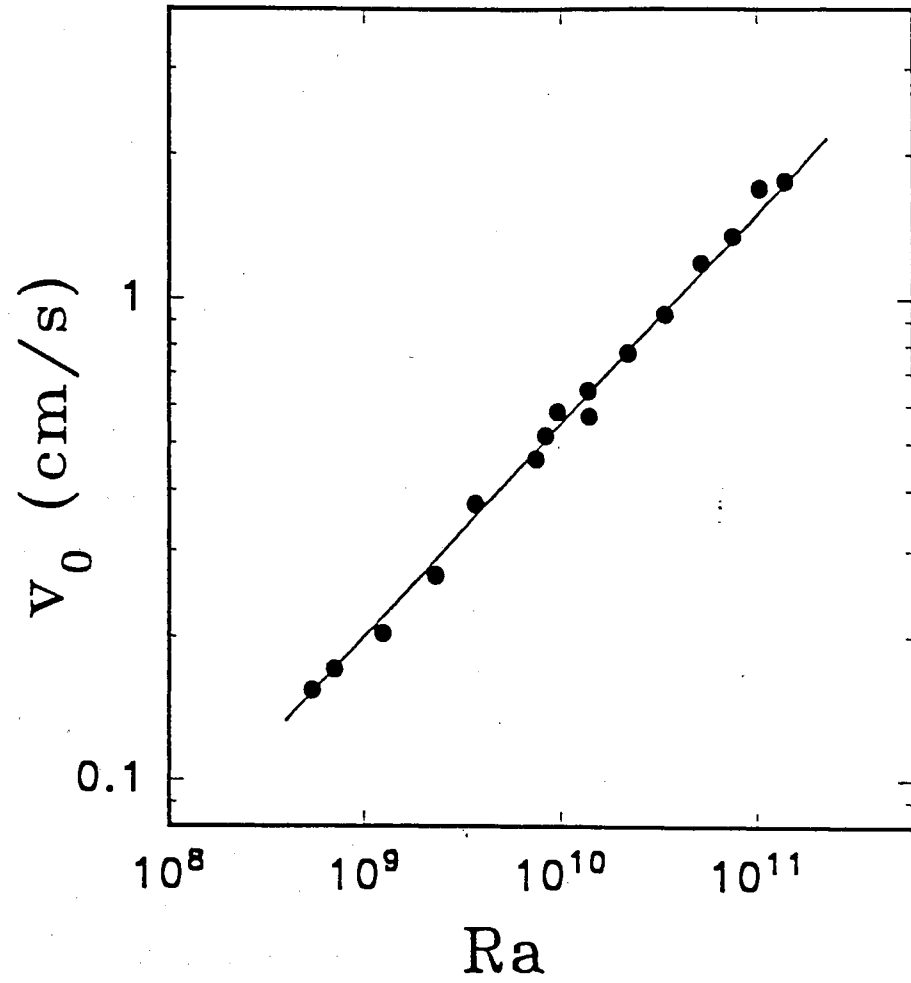
Figure 25. The measured local velocity fluctuations as a function of Ra when the laser beam was horizontally shone through the center of the cells, with $A = 1.0$ and $A = 0.5$. The solid lines are the power-law fit $2.2 \times 10^{-5} Ra^{0.44}$ to the solid circles.

measuring small velocity fluctuations and limited statistics were reported in these measurements. Our new scattering technique used in this experiment, on the other hand, is capable of measuring the velocity PDF with a large dynamic range and a high statistical accuracy.

The above velocity measurements reveal that, in the hard turbulence regime, velocity fluctuations are isotropic and their PDF has an invariant Gaussian form. These findings are consistent with visual observations of the temperature field that, in the hard turbulence regime, thermal plumes emitted from the boundary layers are broken into small structures, as a result of strong turbulent mixing, before traversing through the center region of the cell [29].

An important question one might ask is how the local velocity fluctuates in the soft turbulence regime, where the thermal plumes are found to span the full height of the convection cell [29]. To answer this question, we now examine the measured $G_c(t)$ in the cell with $A = 3$. The shorter cell was used to reduce Ra and to allow the thermal plumes to traverse into the center region easily. As shown in Figure 23, when the laser beam is vertically shone through the cell center, the measured $G_c(t)$ in the soft turbulence regime has the same Lorentzian form as that measured in the hard turbulence regime. When the laser beam is horizontally shone through the cell center (see Figure 22), however, the measured $G_c(t)$ continuously changes its functional form as Ra is increased from 1.2×10^7 to 2.0×10^8. At lower Ra the measured $G_c(t)$ has a Lorentzian tail at large t, but its initial decay is slower than a Lorentzian function. As Ra is increased, the initial part of $G_c(t)$ approaches the Lorentzian form.

To characterize the decay of a non-Lorentzian $G_c(t)$, we measure the half-decay time $T_{1/2}$ of $G_c(t)$. For a Lorentzian function, the half-decay time $T_{1/2} = 1/\Gamma$. Figure 26 compares the measured v_0 ($= \sigma/T_{1/2}$) for the horizontal beam (solid circles) with that for the vertical beam (open circles) at different Ra. The solid line in Figure 26 is an attempted power law fit

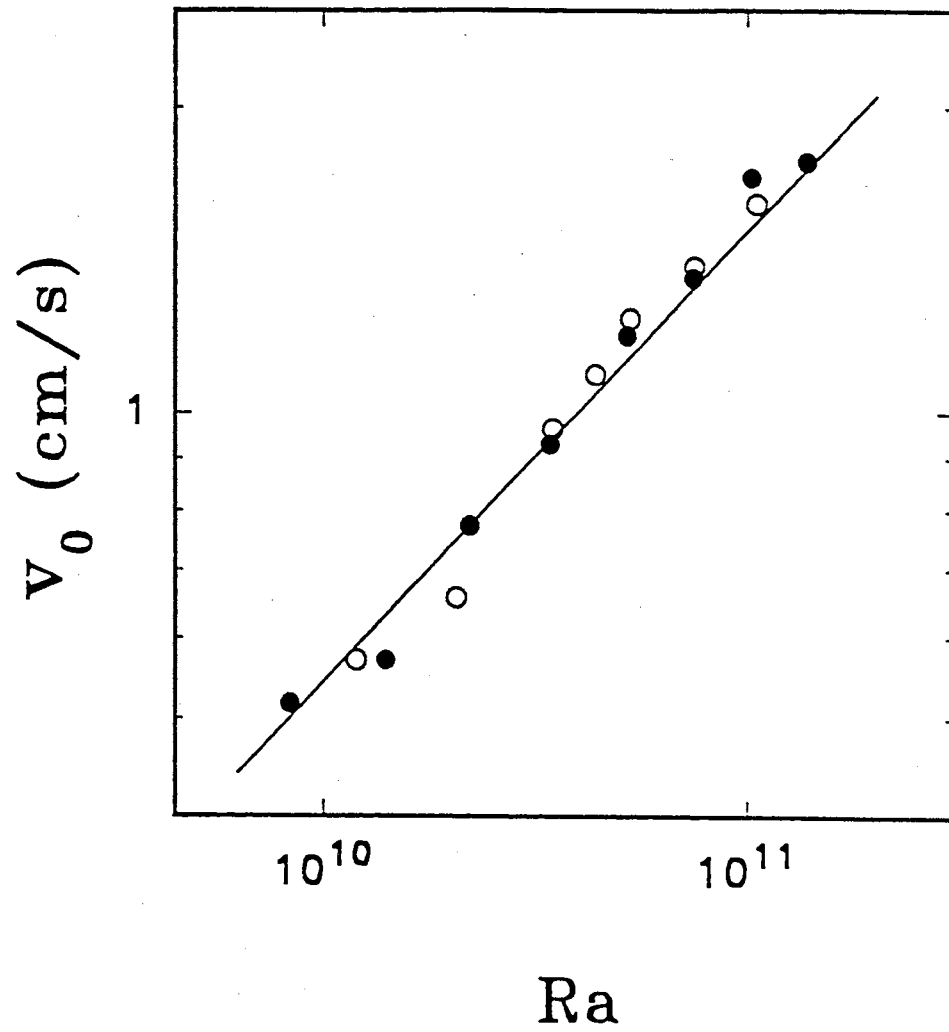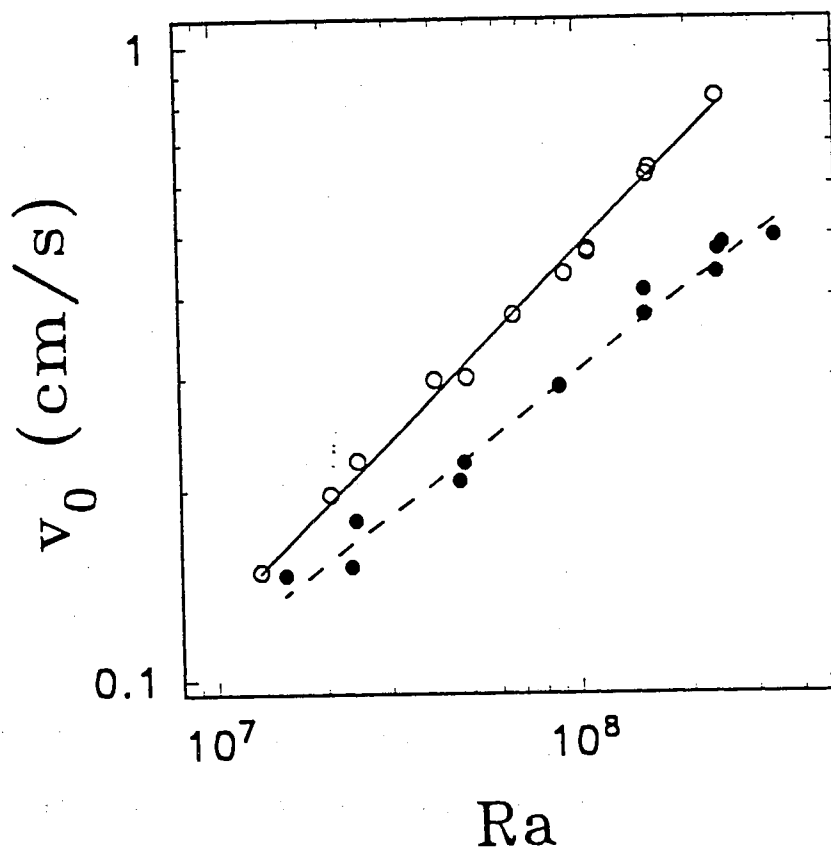$$v_0 = 1.1 \times 10^{-5} Ra^{0.58} \, (cm/s) \tag{87}$$

Figure 26. The measured local velocity fluctuations as a function of Ra for the vertical beam (open circles) and for the horizontal beam (solid circles) with $A = 3$. The solid line is an attempted power-law fit $1.1 \times 10^{-5} Ra^{0.58}$ to the open circles, and the dashed line is an attempted power-law fit $1.0 \times 10^{-4} Ra^{0.44}$ to the solid circles.

to the open circles, and the dashed line is an attempted power-law fit

$$v_0 = 1.0 \times 10^{-4} Ra^{0.44} \, (cm/s) \qquad (88)$$

to the solid circles. Note that the fitted power law for the open circles differs from that obtained in the hard turbulence regime. Furthermore, the power law fits in Figure 26 are different from each other, both in amplitude and in exponent. Figure 26 thus suggests that, in the soft turbulence regime, velocity fluctuations in the vertical direction parallel to gravity differ substantially from those in the horizontal directions. From the measurements in the cell with $A = 3$, we conclude that in the soft turbulence regime the PDF's for the vertical velocity fluctuations do not have a universal form and appear to depend on the coherence of thermal plumes emitted from the boundary layers.

<center>Turbulent Convection Over Rough Surfaces</center>

The rough cell condition was made by replacing the smooth upper and lower plates of the cell with two brass plates, which had woven V-shaped grooves on the surface. As discussed in Chapter III, this experiment is motivated by recent studies of the effects of coherent structures on the transport property of a turbulent fluid [6][7][27]. Thermal plumes and the large-scale circulation have been observed as two main coherent structures in turbulent convection. The question is which plays the major role in carrying the heat away. As we have discussed in Chapter II, there are two theoretical models, which represent the main stream of the recent work. One assumes no thermal plumes involved in the heat transport [27] and the other takes no account of the effect of the large-scale circulation [6]. To understand the real mechanism of the heat transport in turbulent convection, Solomon *et al.* have conducted an experiment, in which they artificially introduced a flow beneath the lower thermal boundary layer by using a moving boundary of mercury under the convecting fluid. Oscillatory shear substantially alters the structure of the thermal plumes, with minimal effect on the heat flux. This result appears to be inconsistent with the marginal stability theory by Kadanoff and his coworkers. With Solomon's

experiment and our own velocity measurements discussed in the last section, can we conclude that the large scale circulation plays the dominant role in carrying the heat through the cell? With this question in mind, we conducted a new convection experiment with a different boundary condition, i.e. both the upper and lower surfaces of the cell are changed to the rough surfaces. Figs. 27 and 28 compare the measured Nusselt number $Nu(Ra)$ (the normalized heat flux) in the rough cells (open circles) with that in the smooth cells (solid triangles). The measurements were conducted in the cells with $A = 0.5$ (see Figure 27) and $A = 1.0$ (see Figure 28). The measured $Nu(Ra)$ in both smooth cells is well described by the power law (solid lines)

$$Nu = 0.16 Ra^{\beta}. \tag{89}$$

The scaling exponent $\beta = 0.281 \pm 0.015$, which agrees well with previous measurements. The measured heat flux in the rough cells is found to be the same as that in the smooth cells for small values of Ra. When Ra becomes larger than a transition value Ra_0, the measured Nu is increased by $\sim 20\%$ as compared with that in the smooth cells. It is seen from Figs. 27 and 28 that the onset of the enhanced heat transport occurs at $Ra_0 \simeq 4 \times 10^8$ in the $A = 1.0$ cell and at $Ra_0 \simeq 5 \times 10^9$ in the $A = 0.5$ cell. It is notable that in the limited range of Ra ($> Ra_0$), the rough cell data can also be described by the power law

$$Nu = 0.19 Ra^{\beta}, \tag{90}$$

where the exponent β is the same as that for the smooth cells, but the amplitude is changed from 0.16 to 0.19 (dashed lines).

To judge the effect of the surface toughness on the heat transport, one needs to compare the roughness height h_R with the thermal boundary layer thickness $\delta_{th}(Ra)$. When h_R is small compared with δ_{th}, the rough elements on the surface are buried beneath the thermal boundary layer, and hence the effect of the surface roughness will be small. This happens in the lower Ra region, where $Ra < Ra_0$. In the opposite limit of large Ra, where $h_R > \delta_{th}$, the surface roughness will strongly affect temperature fluctuations near the surface and thereby alters the

Figure 27. The measured Nu as a function of Ra in the rough cells (open cir-
cles) and in the smooth cells (solid triangles) with $A = 0.5$. The
solid line is an attempted pow-law fit $Nu = 0.16 \times Ra^{0.281}$ to the
solid triangles, and tthe dashed line is an attempted power-law fit
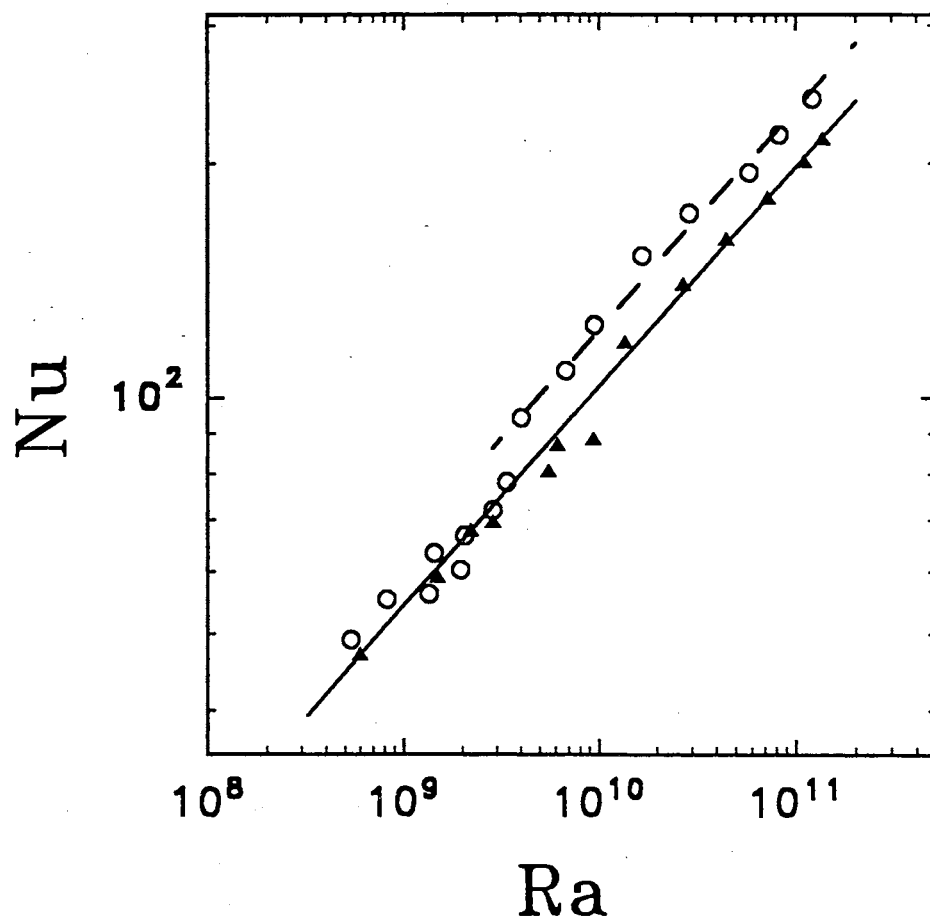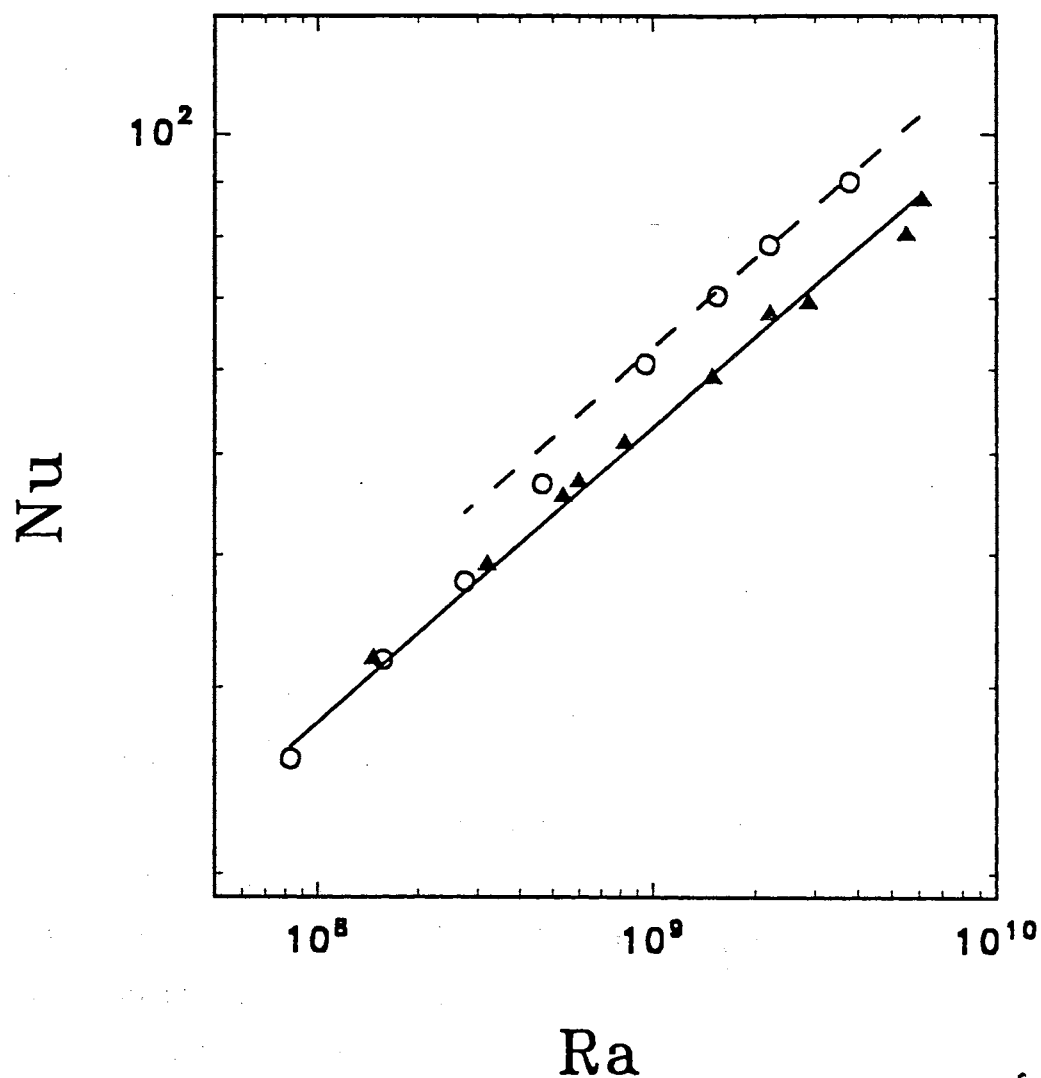$Nu = 0.19 \times Ra^{0.281}$.

Figure 28. The measured Nu as a function of Ra in the rough cells (open circles) and in the smooth cells (solid triangles) with $A = 1.0$. The solid line is an attempted pow-law fit $Nu = 0.16 \times Ra^{0.281}$ to the solid triangles, and tthe dashed line is an attempted power-law fit $Nu = 0.19 \times Ra^{0.281}$.

heat transport. Clearly there will be a transition region between the two extreme limits. The values of δ_{th} can be calculated from the measured Nu using the well-tested relation $\delta_{th} = h/(2Nu)$ [1]. At the transition Rayleigh number ($Ra_0 \simeq 4 \times 10^8$ for the $A = 1.0$ cell and $Ra_0 \simeq 5 \times 10^9$ for the $A = 0.5$ cell), we find the $\delta_{th} \simeq 2.4\,mm$ for both smooth cells. The corresponding length ratio $\delta_{th}/h_R \simeq 0.8$ is close to unity. Figs. 27 and 28 thus support the above arguments for the onset of the enhanced heat transport.

To further understand the mechanism for the enhanced heat transport in the rough cells, we measure the local velocity v and its statistics in the central region using the ICS technique [36]. The experimental setup and apparatus have been detailed in Chapter III. Figs. 29 and 30 show the measured $G_c(t)$ in the rough cells at various values of Ra, when the laser beam was shone through the cell center horizontally (Figure 29) and vertically (Figure 30). As discussed in the previous section, the two beam orientations actually probe different components of the local velocity. In the former case (horizontal beam) the velocity components in the vertical direction and in one of the horizontal directions are measured, whereas in the latter case (vertical beam) only the horizontal components of the local velocity are measured. It is seen from Figure 30 that the functional form of $G_c(t)$ for the vertical beam is well described by the Lorentzian function $1/[1 + (\Gamma t)^2]$ (solid curve), and only the decay rate Γ changes with Ra. Plots of $G_c(t)$ at different Ra superimpose with each other once the time axis is scaled by Γ. As discussed in the last section, the PDF, $P_2(v_i, v_j)$, can be obtained by a simple Laplace inversion of measured $G_c(t)$. For a Lorentzian $G_c(t)$, we find the corresponding $P_2(v_i, v_j)$ is of the Gaussian form $P_2(v_i, v_j) = \frac{1}{v_0^2} e^{-(v_i^2 + v_j^2)/v_0^2}$, where $v_0 = \Gamma\sigma$ is the rms velocity. In the above, we have used the fact that the velocity fluctuations in the horizontal directions are isotropic. As discussed in the previous section, Gaussian-like velocity PDF's have also been found in the smooth cells [25]. Figure 30 thus suggests that the statistics of velocity fluctuations in the horizontal directions are not strongly influenced by the surface roughness. In contrast to horizontal velocity fluctuations, however, velocity fluctuations in the vertical direction are affected by the surface

Figure 29. The measured cross-correlation function as a function of Γt in the rough cells when the laser beam was horizontally shone through the cell center. The experimental conditions are: $Ra = 1.2 \times 10^{10}$ (circles), 1.2×10^9 (triangles) and 3.4×10^8 (squares) all in the $A = 1.0$ cell. The solid curve is the Lorentzian function.

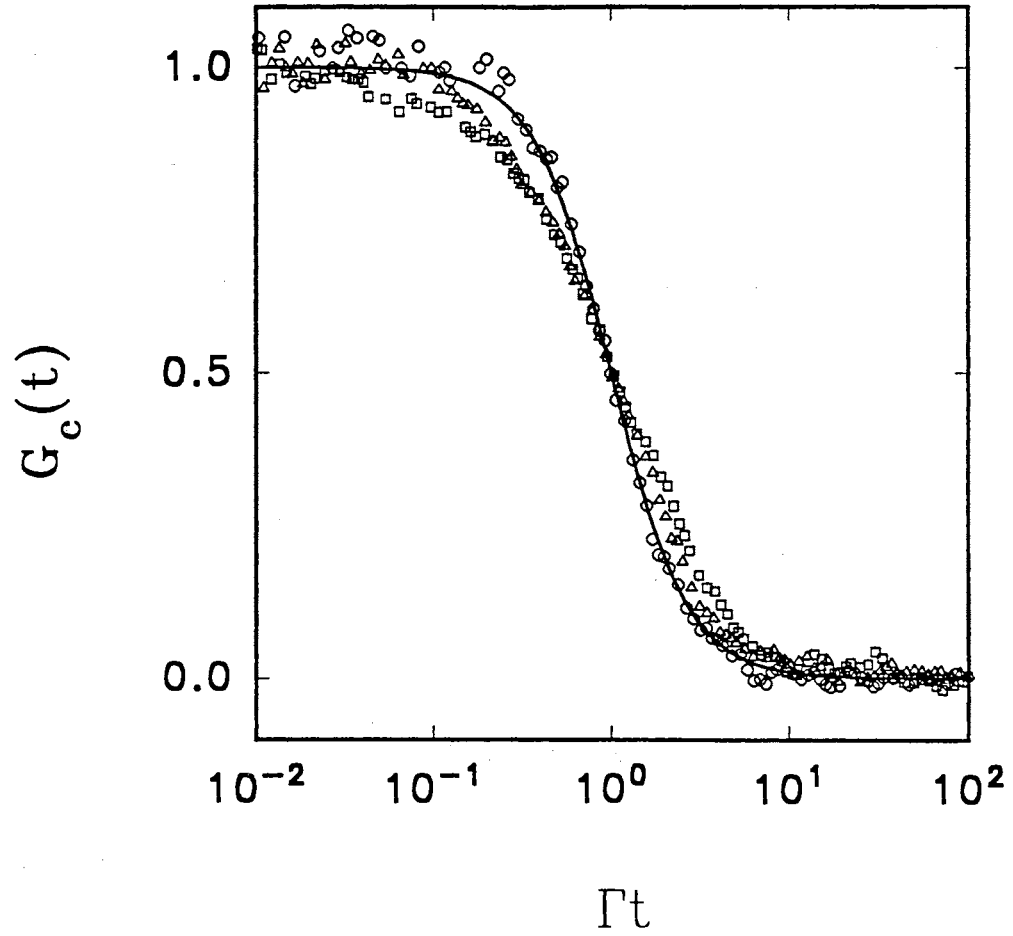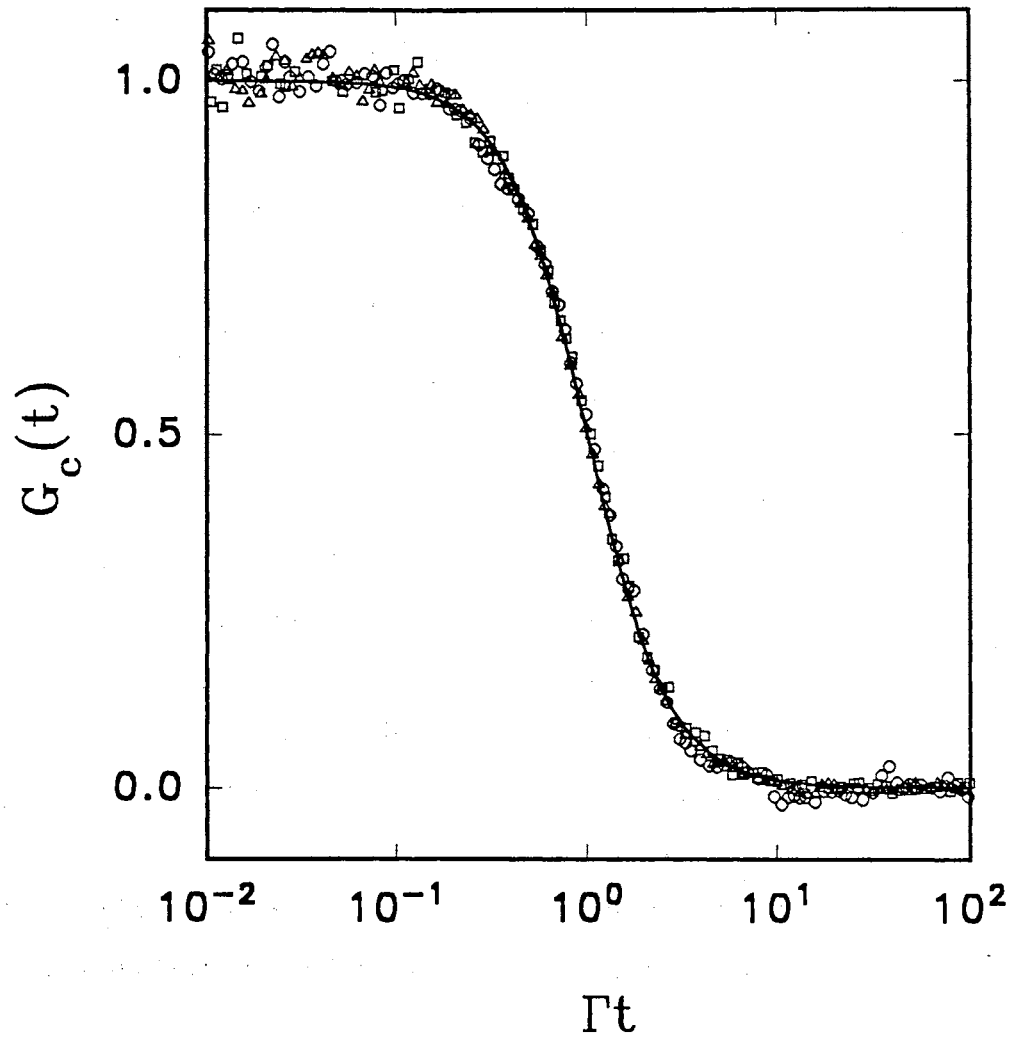Figure 30. The measured cross-correlation function as a function of Γt in the rough cells when the laser beam was vertically shone through the cell center. The experimental conditions are: $Ra = 4.5 \times 10^8$ (triangles), 2.5×10^9 (circles) in the $A = 1.0$ cell and $Ra = 7.0 \times 10^{10}$ (squares) in the $A = 0.5$ cell. The solid curve is the Lorentzian function.

roughness. As shown in Figure 29, when the laser beam is horizontally shone through the cell center, the measured $G_c(t)$ changes its functional form as Ra is increased. Near the transition Rayleigh number $Ra_0 \simeq 4 \times 10^8$, the decay of $G_c(t)$ is slower than a Lorentzian function. When Ra becomes much larger than Ra_0, $G_c(t)$ approaches the Lorentzian form (solid curve). This behavior is found in both rough cells with $A = 0.5$ and $A = 1.0$.

To characterize the decay of a non-Lorentzian $G_c(t)$, we measure the half-decay time $T_{1/2}$ of $G_c(t)$. With the measured σ and Γ (or $T_{1/2}$), we now plot the rms velocity $v_0 = \sigma\Gamma = \sigma/T_{1/2}$ as a function of Ra in Figure 31 (for $A = 0.5$ cell) and Figure 32 ($A = 1.0$ cell). These two figures compare the measured v_0 for the vertical beam (solid circles) with that for the horizontal beam (open squares) at different Ra in the rough cells. It is seen that the convective flow changes its characteristic when Ra reaches the transition Rayleigh number Ra_0. The values of Ra_0 found in the Figs. 31 and 32, i.e., $Ra_0 \simeq 4 \times 10^8$ for the $A = 1.0$ cell and $Ra_0 \simeq 5 \times 10^9$ for the $A = 0.5$ cell, correspond well with those obtained from the Nu measurements shown in Figs. 27 and 28. When Ra is below the transition number (i.e., when $h_R < \delta_{th}$), velocity fluctuations in different directions have the same rms velocity, suggesting that the flow in the central region is isotropic. As discussed in the last section, our velocity experiments [25] in the smooth cells have revealed that in the hard turbulence regime ($Ra > 10^8$), velocity fluctuations are isotropic and the measured v_0 (for both horizontal and vertical beam orientations) obeys the power law

$$v_0 = 2.2 \times 10^{-5} Ra^{0.44} \, (cm/\sec). \tag{91}$$

The solid line in Figure 31 shows the above equation. If the Peclet number Pe $(= v_0 h/\kappa_d)$ is chosen as the dimensionless velocity, the power law becomes

$$Pe = 0.30 \times Ra^{0.44}. \tag{92}$$

Figure 31 shows that the values of v_0 obtained in the rough cell coincide with those in the smooth cell, when the Rayleigh number is smaller than the transition value Ra_0. This observation further supports our argument that when the roughness

Figure 31. The measured local velocity as a function of Ra for the vertical beam (solid circles) and for the horizontal beam (open squares) in the rough cells with $A = 0.5$. The solid line is an attempted power-law $2.2 \times 10^{-5} Ra^{0.44}$. The long dashed line $1.4 \times 10^{-5} Ra^{0.44}$. The short dashed line $3.0 \times 10^{-5} Ra^{0.44}$.
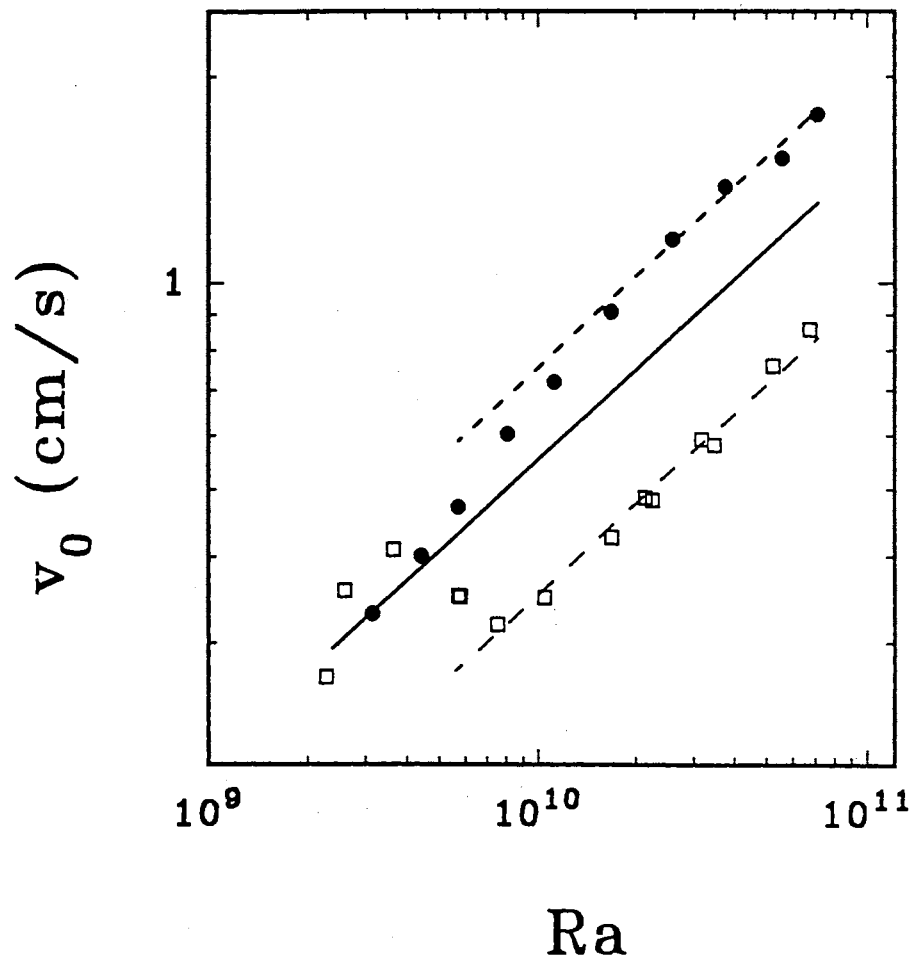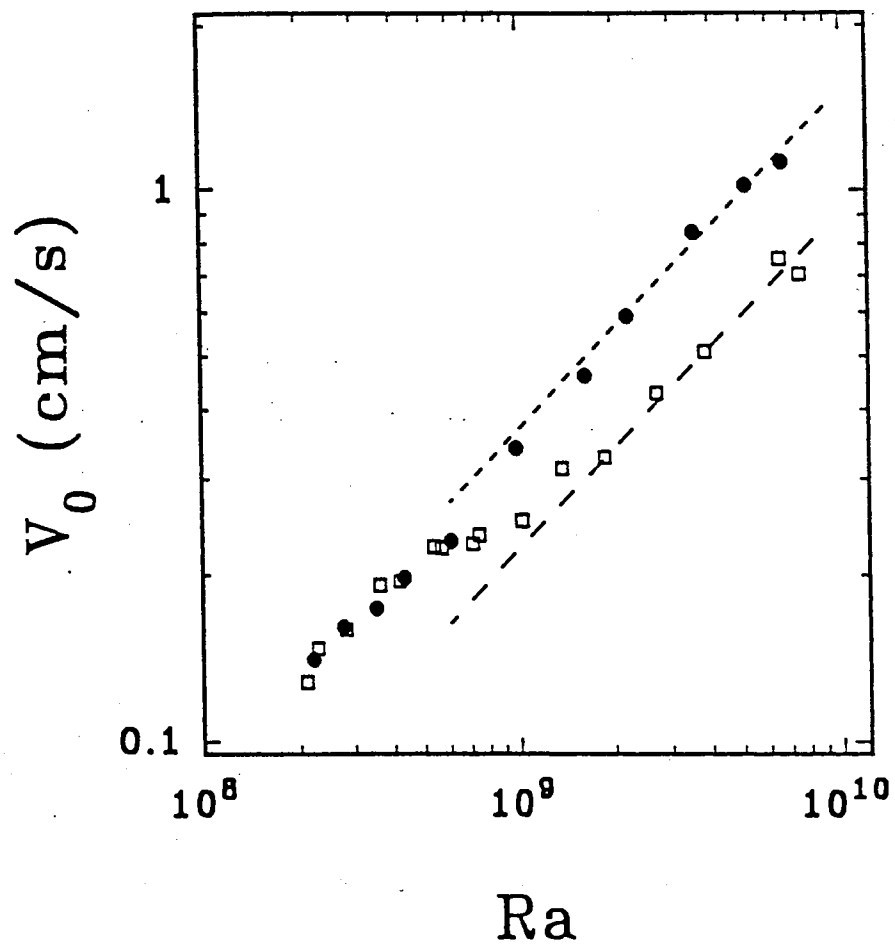
Figure 32. The measured local velocity as a function of Ra for the vertical beam (solid circles) and for the horizontal beam (open squares) in the rough cells with $A = 1.0$. The long dashed line is an attempted power-law fit $0.73 \times 10^{-6} Ra^{0.61}$. The short dashed line $1.2 \times 10^{-6} Ra^{0.61}$.

height h_R is lower than the thermal boundary layer thickness δ_{th}, the flow in the rough cell should behave the same as that in the smooth cell.

When the Rayleigh number becomes larger than Ra_0, the measured v_0 in the rough cell deviates from that in the smooth cells, and it also changes with the beam orientation. It is seen from Figs. 31 and 32 that the surface roughness affects the vertical velocity fluctuations (horizontal beam) more than the horizontal velocity fluctuations (vertical beam). The dashed lines in Figure 31 are the attempted power law fits $1.4 \times 10^{-5} Ra^{0.44}$ (long-dashed line), $3.0 \times 10^{-5} Ra^{0.44}$ (short-dashed line), and those in Figure 32 are $0.73 \times 10^{-6} Ra^{0.61}$ (long-dashed line), $1.2 \times 10^{-6} Ra^{0.61}$ (short-dashed line). Note that the power law fits in Figs. 31 and 32 are different among themselves both in amplitude and in exponent. Figs. 31 and 32 thus indicate that velocity fluctuations in the vertical direction parallel to gravity become substantially different from those in the horizontal directions, once the flow feels the surface roughness (i.e., when $h_R < \delta_{th}$). This anisotropic behavior of velocity fluctuations in the rough cells at large Ra ($> Ra_0$) is very similar to that found in the smooth cells [25] at small Ra. As discussed in the last section, when Ra is in the soft turbulence regime, the thermal plumes span the full height of the cell [29]. By comparing the velocity measurements with the Nu measurements, we find that the anisotropic behavior of velocity fluctuations in the central region is directly related to the enhanced heat transport as shown in Figs. 27 and 28.

From the temperature and velocity measurements in the rough and smooth cells, we conclude that the main effect of the surface roughness is to increase the emission of large thermal plumes from the interstices between the roughness elements, and these large thermal plumes travel vertically from the boundary into the cell center. The extra thermal plumes produced by the surface roughness enhance the heat transport, and they are also responsible for the anisotropic behavior of velocity fluctuations in the central region. Similar increase in intermittent bursting of coherent structures is also found in the wind tunnel with rough walls [11][15].

Our experiment reveals that the influence of the surface roughness is not only confined to the near-wall region, but also extended into the central region of the cell. When the flow feels the surface roughness, the power law behavior of velocity fluctuations is changed considerably, even though the exponent β for the normalized heat flux Nu remains unchanged. It appears that the scaling behavior of velocity fluctuations (and temperature fluctuations) in the center region is very sensitive to the detail structure of turbulence, whereas the power law exponent β for Nu is not. The striking effects of the surface roughness provide new insights into the roles of the thermal plumes played in determining the heat transport in turbulent convection. Our experiment in the rough cells indicates that both the large-scale circulation and thermal plumes contribute to the heat transport in turbulent convection, and their relative weight has little effect in determining the power law exponent β for Nu. The discovery of the enhanced heat transport in the rough cells also has important applications in engineering for more efficient heat transfer.

CHAPTER V

SUMMARY

Conclusion

We have studied turbulent convection using the scattering techniques of photon correlation spectroscopy (HCS) and incoherent cross-correlation spectroscopy (ICS). Measurements of the intensity correlation function $g_c(t)$ give access to the information about spatial and temporal fluctuations of the local velocity field in turbulent convection. The Rayleigh number Ra, which is the control parameter in our experiment, is varied from 10^7 to 10^{11}. Scaling laws in the velocity statistics and in the scale-dependence of the velocity difference are found in the hard turbulence regime of turbulent convection. Notable changes are observed when rough upper and lower surfaces are introduced to the convection cell. Our experiment produces a benchmark against which future theoretical models can be tested.

With the HCS scheme, we have measured the intensity auto-correlation function $g_{coh}(t)$, whose decay rate $\Gamma \sim qu(l)$ can be used to probe the velocity difference $\delta v(l)$ at various length scales l. The measured $g_{coh}(t)$ is found to be of the scaling form $g[qu(l)t]$, with $u(l) \sim l^{0.6}$ being the characteristic turbulent velocity at the length scale l and in the direction of the scattering vector q. The measured power-law exponent in $u(l)$ agrees well with the recent theoretical predictions by L'vov [18], Zeitak and Procaccia [22]. Our measurements suggest that the probability density function $P(\delta v, l)$ for the velocity difference $\delta v(l)$ has the scaling form $Q[\delta v/u(l)] / u(l)$. It is found that fluctuations of the velocity difference are isotropic at the center of the convection cell. It is also found that there exists a cutoff length l_c below which the velocity difference scales differently from that in the inertial range. The Rayleigh number dependence of the cutoff length l_c

is similar to that of the thermal boundary layer thickness δ. This indicates that the measured cutoff length l_c in the velocity scaling is determined by the smallest length scale of the coherent structures in the core region of turbulent convection.

Using the ICS technique we have measured the local velocity v and its probability density functions $P(v)$. Previous temperature measurements have revealed two distinct turbulent states in convection: soft turbulence when $Ra < 4 \times 10^7$ and hard turbulence for $Ra > 4 \times 10^7$. Our velocity measurements show that local velocity fluctuations at the center of the convection cell are isotropic in the hard turbulence regime, and their probability density functions in the center region have an invariant Gaussian form $P(v) = (1/v_0^2) \exp[-(v/v_0)^2]$. The rms velocity $v_0 \sim Ra^{0.44}$, which is in good agreement with the theoretical predictions [6][27]. In the soft turbulence regime, on the other hand, velocity fluctuations in the vertical direction parallel to gravity differ substantially from those in the horizontal direction. The probability density functions for the vertical velocity fluctuations do not have a universal form and appear to depend on the coherence of thermal plumes emitted from the boundary layers. The probability density functions for the horizontal velocity fluctuations remain an invariant Gaussian form.

The Nusselt number Nu has been measured as a function of the Rayleigh number in both the "smooth" and "rough" cells. It is found that the vertical heat flux is increased by $\sim 20\%$ in the rough cells, when the Rayleigh number becomes larger than a transition value. The transition occurs when the thermal boundary layer thickness becomes comparable with the height of the surface roughness. It is observed that the influence of the surface roughness is not only confined to the near-wall region, but also extended into the central region of the cell. The experiment reveals that the main effect of the surface roughness is to increase the emission of large thermal plumes, which travel vertically through the central region. These extra thermal plumes enhance the heat transport, and they are also responsible for the anisotropic behavior of velocity fluctuations in the cell center.

Future Work

One promising path for the study of turbulent convection is to exploit the aspect ratio parameter. As discussed in Chapter II, there are three control parameters for thermal convection: the Rayleigh number Ra, the Prandtl number Pr, and the aspect ratio A of the convection cell. In the experiments described in this thesis, we have continuously varied Ra while we kept Pr (~ 1) and A constant. Because it is very difficult to continuously vary the Prandtl number and at the same time keep Ra constant using common fluids, we are unable to study the effect of Pr at this point. However, it is possible to study how the aspect ratio A affects turbulence states and the associated coherent structures. An experimental setup can be designed to change A continuously for a given temperature difference between the upper and lower plates. When $A \ll 1$ (i.e., for a tall tube), the large-scale circulation will dominant the heat transport whereas the effect of the thermal plumes will be limited to the region near the upper and lower plates. In the opposite limit $A \gg 1$, where the distance between the upper and lower plates is much smaller than the diameter of the cell, the thermal plumes will play the dominant role in carrying the heat away and the large-scale circulation will be completely suppressed. The study of the temperature and velocity fluctuations in the above two extreme limits and in the transition region between these two limits will provide new insights toward the further understanding of some important issues. These issues include: (1) is the soft turbulence state a universal phenomenon or is it a simple transition state towards the universal hard turbulence regime? (2) What is the origin of the large-scale circulation? (3) What are the relative contributions of the large-scale circulation and the thermal plumes to the turbulent heat transport? A systematic study of the aspect ratio effect will answer these unsolved questions.

In the experiment discussed in Chapter IV, we have carried out the measurements of the local velocity and the heat flux in a cell with rough upper and lower surfaces. The velocity measurements were only conducted at the center of

the cell. A more extensive study of convective turbulence in the rough cells should be conducted in the future. One can first measure the velocity difference $\delta v(l)$ over various length scales in the rough cells. An anisotropic behavior similar to that found for the local velocity fluctuations is expected for $\delta v(l)$. One can also measure temperature fluctuations and their PDF's in the central region of the rough cell. Previous temperature measurements in the smooth cell have shown that the temperature PDF changes its functional form when the thermal plumes traverse through the cell center vertically [12][29]. Similar transition for the velocity field has also been observed in the rough cell, when the Rayleigh number approach a transition value Ra_0. I speculate that in the rough cell the temperature PDF will remain a simple exponential form for $Ra < Ra_0$, and it will be altered when Ra becomes larger than Ra_0, in which case the surface roughness will produce extra thermal plumes. With the ability to perturb the boundary layers and to alter the resulting eruptions of the thermal plumes, one will be able to examine how the surface roughness affects the boundary layers, the spatial structure of the large-scale circulation, and the temperature and velocity statistics.

Another important but unanswered question in the study of convective turbulence is how the temperature field interacts with the velocity field. This question is directly related to the physical mechanisms for the heat transport and the energy cascade in turbulent convection. In mixing length theory [6], the velocity field is usually assumed to coupled to the temperature field through a free-fall velocity $v_c \sim (\alpha g \delta T h)^{\frac{1}{2}}$ [6]. However, our velocity measurements at the central region of the cell [26] show that the velocity PDF's are not directly correlated with the temperture PDF's. To understand the correlation between the temperature and velocity fields, one needs to conduct simultaneous temperature and velocity measurements, from which the temperature-velocity cross-correlation function can be obtained. In the experiment, one can use LDV (with some changes in optics [37]) to measure the flow velocity and a thermistor to sense the fluid temperature. The simultaneous temperature-velocity measurements will complement the individual temperature and velocity measurements conducted in recent years. Furthermore,

the experiment may find new scaling laws for the cross-correlation function, and provide a body of reliable data, with which one can build new theoretical models to understand the nature of convective turbulence.

BIBLIOGRAPHY

1. A. Belmonte, A. Tilgner, and A. Libchaber, Phys. Rev. Lett. **70**, 4067 (1993); Phys. Rev. E **47**, R2253 (1993).

2. A. Belmonte, A. Tilgner, and A. Libchaber, Phys. Rev. E **50**, 269 (1994).

3. B. J. Berne and R. Pecora, Dynamic Light Scattering (Wiley, New York, 1976).

4. R. Bolgiano, J. Geophys. Research **64**, 2226 (1959).

5. B. M. Boubnov, and G. S. Golitsyn, Convection in Rotating Fluids (Kluwer, Dordrecht, 1995).

6. B. Castaing et al., J. Fluid Mech. **204**, 1 (1989).

7. F. Chillá, S. Ciliberto, and C. Innocenti, Europhys. Lett. **22**, 681 (1993).

8. U. Frisch, P. Sulem, and M. Nelkin, J. Fluid Mech. **87**, 719 (1978).

9. G. G. Fuller, J. M. Tallison, R. L. Schmidt, and L. G. Leal, J. Fluid Mech. **100**, 555 (1980).

10. A. M. Garon and R. J. Goldstein, Phys. Fluids **11**, 1818 (1973).

11. A. J. Grass, J. Fluid Mech. **50**, 233 (1971); A. J. Grass, R. J. Stuart, and M. Mansour-Tehrani, AIAA J. **31**, 837 (1993).

12. F. Heslot, B. Castaing, and A. Libchaber, Phys. Rev. A **36**, 5870 (1987).

13. A. N. Kolmogorov, C. R. Dokl. Acad. Sci. USSR **30**, 301 (1941); **31**, 538 (1941).

14. R. Kraichnan, Phys. Fluids **5**, 1374 (1962).

15. P.-A. Krogstad, R. A. Antonia, and L. W. B. Browne, J. Fluid Mech. **245**, 599 (1992); P.-A. Krogstad and R. A. Antonia, J. Fluid Mech. **277**, 1 (1994).

16. R. R. Long, Geophys. Fluid Dyn. **6**, 337 (1975).

17. V. S. L'vov and G. E. Falkovich, Weizmann Institute of Science Report No. WIS-91/7/Mar-PH, 1991 (unpublished).

18. V. S. L'vov, Phys. Rev. Lett. **67**, 687 (1991).

19. W. V. R. Malkus, Discrete transtions in turbulent convection, Proc. R. Soc. Lond. A **225**, 185 (1954).

20. W. V. R. Malkus, Outline of a theory of turbulent convection, In Theory and Fundamental Research in Heat Transfer (pergamon, 1963).

21. A. S. Monin and A. M. Yaglom, Statistical Fluid Mechanics: Mechanics of Turbulence (MIT Press, Cambridge, MA, 1975).

22. I. Procaccia and R. Zeitak, Phys. Rev. Lett. **62**, 2128 (1989).

23. Zhen-Su She, Phys. Fluids A **1**, 911 (1989).

24. M. J. Shelley and M. Vinson, Nonlinearity **5**, 323 (1992).

25. Y. Shen, K.-Q. Xia, and P. Tong, Phys. Rev. Lett. **75**, 437 (1995).

26. Y. Shen, and P. Tong, Phys. Rev. Lett. (accepted for publishing in 1996).

27. B. I. Shraiman and E. D. Siggia, Phys. Rev. A **42**, 3650 (1990).

28. E. D. Siggia, Annu. Rev. Fluid Mech. **26**, 137 (1994).

29. T. H. Solomon and J. P. Gollub, Phys. Rev. Lett. **64**, 2382 (1990); Phys. Rev. A **43**, 6683 (1991).

30. H. Tanaka and H. Miyata, Int. J. Heat Mass Transfer **23**, 1273 (1980).

31. A. Khurana, Physcis Today, **17**, June 1988.

32. P. Tong *et al.* (to be published).

33. P. Tong, W. I. Goldburg, C. K. Chan, and A. Sirivat, Phys. Rev. A **37**, 2125 (1988).

34. P. Tong and W. I. Goldburg, Phys. Fluids **31**, 2841 (1988).

35. P. Tong, and Y. Shen, Phys. Rev. Lett. **69**, 2066 (1992).

36. P. Tong, K.-Q. Xia, and B. J. Ackerson, J. Chem. Phys. **98**, 9256 (1993).

37. P. Tong and K.-Q. Xia, to be published.

38. D. J. Tritton, Physical Fluid Dynamics, second edition (Clarendon Press, Oxford, 1988).

39. X.-Z. Wu, L. Kadanoff, A. Libchaber, and M. Sano, Phys. Rev. Lett. **64**, 2140 (1990).

40. G. Zocchi, E. Moses, and A. libchaber, Physica A **166**, 387 (1990).

VITA

Yi Shen

Candidate for the Degree of

Doctor of Philosophy

Thesis: VELOCITY FLUCTUATIONS AND THEIR STATISTICS IN TURBULENT CONVECTION

Major Field: Physics

Biographical:

Personal Data: Born in Shanghai, China, on August 1, 1968, the son of Yi-Lan Qian and Xiang-Ming Shen.
Married Jie-Wei Wang, January 3, 1993.

Education: Received Bachelor of Science Degree in Physics from FuDan University, Shanghai, China in July 1989. Completed requirements for the Doctor of Philosophy Degree at Oklahoma State University in May 1996.

Professional Experience: Manager at San-Lee Limited Inc., Macao from July 1989 to August 1990; Teaching Assistant, Department of Physics, Oklahoma State University, from August 1990 to December 1991; Research Assistant, Department of Physics, Oklahoma State University, from January 1992 to present.

Professional Memberships: American Physical Society, Phi Kappa Phi Honor Society.